Circulation conservation in the outflow of warm conveyor belts and consequences for Rossby wave evolution

Leo Saffin[2] | **John Methven[1]** | **Jake Bland[1]** | **Ben Harvey[1, 3]** | **Claudio Sanchez[4]**

[1]Department of Meteorology; University of Reading; UK

[2]Institute for Climate and Atmospheric Science; University of Leeds; UK

[3]National Centre for Atmospheric Science; University of Reading; UK

[4]UK Met Office; Exeter; UK

Correspondence
Leo Saffin; University of Leeds; UK
Email: l.saffin@leeds.ac.uk

Funding information

Rossby waves on the jet stream are associated with meridional motions, displacing air and the strong potential vorticity (PV) gradient on isentropic surfaces. Poleward motion along sloping isentropic surfaces typically results in ascent and a ridge of air with low PV values. Latent heating in the ascending warm conveyor belt (WCB) enables air to cross isentropic surfaces so that the WCB outflow into a ridge occurs in a higher isentropic layer than the inflow. However, the PV impermeability theorem states that there can be no PV flux across isentropic surfaces, so how can heating alter the PV pattern of a Rossby wave? Here, the ways in which heating in WCBs can influence Rossby wave evolution at tropopause level are explained in the context of the PV impermeability theorem.

First, a WCB outflow volume is defined by the upper tropospheric air in a ridge that has experienced net heating over the last few days, using a tracer within short global model forecasts. Second, the boundary of this outflow volume is tracked backwards using isentropic trajectories allowing quantification of the degree to which circulation is conserved, as predicted by theory, even though the WCB transports mass into the volume from lower isentropic layers. This diabatic flux of mass into the outflow volume re-

sults in an increase in density and expansion in outflow area, the partition being determined approximately by PV inversion. The area expansion, combined with conservation of circulation, implies more negative vorticity. The relative vorticity change from divergent outflow can be as large as the decrease relative to the background planetary vorticity associated with poleward displacement of the circuit. The additional anticyclonic relative motion results in enhanced anticyclonic over-turning of PV contours on the eastern flank of the ridge, altering qualitatively the nonlinear evolution of the Rossby wave.

1 | INTRODUCTION

Water in the atmosphere and cloud processes are known to have an important influence on weather system development. For example, latent heat release associated with condensation of water vapour enhances the ascent rate of air masses. Developing mid-latitude baroclinic waves, and their associated cyclones and anticyclones, are amplified by latent heating in ascending air streams (Emanuel et al., 1987). The key mechanism can be understood in terms of the increasing ascent rate resulting in greater vortex stretching at low levels and faster cyclone growth.

In an adiabatic baroclinic wave, poleward motion along isentropic surfaces intersecting the tropopause will result in a "negative PV anomaly" (in the Northern Hemisphere) as a result of material potential vorticity (PV) conservation in the presence of a positive meridional PV gradient. PV values are more negative in the "ridge" that is formed than at other locations with similar latitude and altitude. The negative PV anomaly is associated with lower static stability and anticyclonic relative vorticity, through the PV invertibility principal associated with large-scale balance (Hoskins et al., 1985). It is the pattern of horizontal motion anomalies associated with PV anomalies that gives rise to the Rossby wave propagation mechanism; Rossby waves on a positive meridional PV gradient propagate westwards relative to the zonal flow.

De Vries et al. (2010) extended the adiabatic quasi-geostrophic theory for baroclinic growth in terms of counter-propagating Rossby waves (Bretherton, 1966; Hoskins et al., 1985; Heifetz et al., 2004) to a general framework with diabatic heating linked to vertical velocity. This applies to the general initial value problem for the growth of wave-like disturbances on unstable zonal jets, including variation with latitude and height on the sphere (Methven et al., 2005). Two ways of coupling heating to vertical velocity are employed by De Vries et al. (2010), described as "wave-CISK" (a form of "cumulus heating parametrization") and "large-scale rain", but the general results in terms of growth rates are similar.

The question addressed here is how the latent heating in ascending air streams can influence Rossby wave disturbances at tropopause level and their subsequent development. The majority of ascending motion, condensation and latent heat release within cyclones occurs within the warm conveyor belt (WCB) air stream. A WCB is a flow of air

from the warm sector of a cyclone transporting air poleward, parallel to, and ahead of, the cyclone's cold front (Harrold, 1973). The WCB ascends along the isentropic slope into the developing ridge of a Rossby wave and diabatic heating enables the air to cross potential temperature (θ) surfaces, so that the WCB outflow is at significantly higher θ-surfaces than the inflow. The impact of diabatic heating on WCB ascent is large: on average WCB air parcels experience a net diabatic heating of ≈ 20 K (Madonna et al., 2014).

Grams et al. (2011) and Grams and Archambault (2016) describe how the horizontally divergent flow resulting from the "diabatic mass transport" into these higher isentropic layers advects the tropopause further away from the outflow centre, therefore building the tropopause ridge by extending it horizontally and therefore increasing ridge amplitude relative to a notional adiabatic flow. Methven (2015) argued theoretically that the Kelvin's circulation of the upper tropospheric WCB outflow volume should be almost unaffected by the diabatic mass transport into it. This result stems from the PV impermeability theorem of Haynes and McIntyre (1990) which states that there can be no PV flux across isentropic surfaces. The argument will be summarised here in Section 2. What influence can a WCB have on Rossby wave disturbances at the tropopause if it has no influence on circulation in the isentropic layer of the outflow? This paper sets out to answer this question by quantifying what happens to mass transport, circulation and relative vorticity in observed cases of WCB outflow into the ridges of Rossby waves propagating along the jet stream at tropopause level.

The impact of diabatic heating in WCBs on the negative PV anomaly in upper tropospheric ridges is a subtle problem. From a Lagrangian perspective, air mass trajectories following the resolved 3-D flow in a WCB will experience an increase in PV between the boundary layer inflow and the level of the latent heating maximum and then a decrease in PV as air rises above the heating into the outflow. However, from the Lagrangian form of the evolution equation for Ertel PV (P):

$$\frac{DP}{Dt} = \frac{1}{\rho} \left\{ \boldsymbol{\zeta}.\nabla Q + \nabla\theta.\nabla \times \mathbf{F} \right\} \tag{1}$$

it is not possible to anticipate how much the initial increase in PV is outweighed by the subsequent decrease (since quantification depends on knowing the scalar product between absolute vorticity and heating gradient). Note that ρ is air density, $\boldsymbol{\zeta}$ is the absolute vorticity vector, Q is the diabatic heating rate $D\theta/Dt$, θ is potential temperature and $\mathbf{F}$ denotes frictional forces in the momentum equation. However, Madonna et al. (2014) found from a 30-year Lagrangian climatology that the PV of the outflow approximately equals the PV of the inflow in WCB composites. While the mid-level PV maximum can be important for intensifying the parent cyclone (Ahmadi-Givi et al., 2004), these results suggest that the changes in the absolute value of PV are less important for the negative PV anomaly (and anti-cyclonic relative motion) than the enhanced ascent and higher location of the outflow volume (therefore more anomalously negative compared with elsewhere at the same latitude and altitude). Nevertheless, the strength of the diabatic heating in the WCB strongly impacts the development of the ridge and has been shown to be important for the downstream development of cyclones (Schemm et al., 2013) and blocking (Pfahl et al., 2015). Recently, Sánchez et al. (2020) have also shown that periods when diabatic influence on the horizontal advection of the tropopause, and associated ridge building across the North Atlantic, are stronger than normal are linked to lower predictability than usual for weather over Europe and "predictability barriers" where forecast error grows more rapidly than ensemble forecast spread. In other words, forecasts (at lead times greater than 2 days) are more uncertain when diabatic processes affect the tropopause location.

The purpose of this paper is to examine quantitatively diabatic mass transport and changes in circulation and vorticity for cases occurring during the North Atlantic Waveguide and Downstream Impacts Experiment (NAWDEX) campaign period (September-October 2016). Section 2 presents relevant theory for changes in Kelvin's circulation in

the presence of diabatic processes, stemming from integration of the Ertel PV evolution equation, and then summarises of the conceptual WCB model of Methven (2015). This enables formulation of the detailed questions that will be answered using global model data for the observed NAWDEX cases. In section 3 the Met Office global model data (3.2) and trajectory calculations (3.3) are described, as well as the synoptic situations associated with the NAWDEX cases. In section 4 the WCB outflow (4.1) and inflow (4.3) volumes are identified objectively from the model data. Integral properties are calculated for these control volumes and the evolution of these measures is described (4.4). In section 5 conclusions are drawn from the analysis of the integral properties of WCB outflow and inflow.

2 | THEORY

2.1 | Effects of heating in the PV and circulation equations

Constraints on the influence of diabatic processes on Kelvin's circulation as a consequence of the PV impermeability theorem (Haynes and McIntyre, 1990) are derived here without approximation. Then the isentropic coordinate version, valid with the hydrostatic approximation, is introduced that will be used to calculate the results of the paper. Start from the Ertel PV equation in flux form:

$$\frac{\partial}{\partial t}(\rho P) + \nabla \cdot (\rho P \mathbf{u}) + \nabla \cdot \mathbf{J}_{\mathrm{HM}} = 0 \tag{2}$$

where P is Ertel PV, $\mathbf{u}$ is the 3-D velocity vector and $\mathbf{J}_{\mathrm{HM}} = -\zeta Q - \mathbf{F} \times \nabla \theta$ is a flux arising from non-conservative terms, in the form introduced by Haynes and McIntyre (1987). It is useful to manipulate the equation into the form:

$$\frac{\partial}{\partial t}(\rho P) + \nabla \cdot (\rho P \mathbf{V}) + \nabla \cdot \mathbf{J} = 0 \tag{3}$$

where $\mathbf{V} = \mathbf{u} - \mathbf{u}_D$ is the velocity parallel to isentropic surfaces, $\mathbf{u}_D = \mathbf{n} \, Q / |\nabla \theta|$ is the normal velocity across isentropic surfaces and the "non-advective PV flux":

$$\mathbf{J} = -\zeta_{\parallel} Q - \mathbf{F} \times \nabla \theta \tag{4}$$

where $\zeta_{\parallel}$ is the component of absolute vorticity parallel to isentropic surfaces. This yields directly the PV impermeability theorem (Haynes and McIntyre, 1990): the component of the full PV flux normal to isentropic surfaces is identically zero:

$$\{\rho P \mathbf{V} + \mathbf{J}\} \cdot \mathbf{n} = 0 \tag{5}$$

Now integrate the PV equation over a volume bounded by isentropic surfaces above and below and a lateral boundary (the circuit on both isentropic surfaces having the same horizontal projection):

$$\int \iint \frac{\partial}{\partial t}(\rho P) \; dA \, dz \quad = \quad \int \iint -\nabla \cdot (\rho P \mathbf{V} + \mathbf{J}) \; dA \, dz \tag{6}$$
$$= \quad -\int \oint (\rho P \mathbf{V} + \mathbf{J}) \cdot \mathbf{l} \, dl \, dz$$

where Gauss' theorem has been used and the surface integral of the normal component of the advective and

non-advective PV fluxes are taken over the lateral boundaries of the volume ($\mathbf{l}$ is the normal to lateral faces) and the PV impermeability condition (5) has been used. This equation is exact for compressible, non-hydrostatic fluids. However, it is convenient in the later analysis to introduce the usual isentropic coordinate form of the equations (as in Methven (2015)). Using the definition of Ertel PV we can write $\rho P = \boldsymbol{\zeta} . \nabla \theta = \boldsymbol{\zeta} . \mathbf{n} |\nabla \theta|$ and thus:

$$\rho P \, dz = \boldsymbol{\zeta} . \mathbf{n} \, |\nabla \theta| \, dz = \zeta_\theta \, \frac{\partial \theta}{\partial z} \, dz = \zeta_\theta \, d\theta \tag{7}$$

where we have defined $\zeta_\theta = \boldsymbol{\zeta} . \mathbf{n} |\nabla \theta| / (\partial \theta / \partial z)$ as in Section 8.8 of Hoskins and James (2014) and also $d\theta = (\partial \theta / \partial z) \, dz$ so that potential temperature is being used to re-label the vertical coordinate (assuming monotonic variation). Finally, the PV definition can be written:

$$rP = \zeta_\theta \tag{8}$$

where the pseudo-density in isentropic coordinates is defined by $r = \rho \, \partial z / \partial \theta$. To this point no approximation has been made. Consider the typical situation where the vertical gradient of potential temperature is dominated by the gradient in a background profile, $\theta_r(z)$, that is only slowly varying in time then one can take $\partial \theta_r / \partial z$ out of the time derivative in (6) to obtain:

$$\int \iint \frac{\partial}{\partial t} (\zeta_\theta) \, dA \, d\theta \approx - \int \oint \left(\zeta_\theta \mathbf{V} + \hat{\mathbf{J}} \right) . \mathbf{l} \, dl \, d\theta \tag{9}$$

Note that isentropic coordinate equation (9) appears formally similar to the exact form (6). The unit vector $\mathbf{l}$ is horizontal and therefore only the horizontal components of the vectors $\mathbf{V}$ and $\hat{\mathbf{J}} = \mathbf{J}/(\partial \theta_r / \partial z)$ influence the circulation integral. However, consistent with the hydrostatic approximation we assume that $\mathbf{V}.\mathbf{l} \approx \mathbf{V}_h.\mathbf{l}$ (i.e., the projection of the horizontal wind vector onto $\mathbf{l}$ is used) and in the non-advective PV flux (4) we approximate $\zeta_{||}.\mathbf{l} \approx \zeta_h.\mathbf{l}$.

Now allowing for the movement of the lateral boundary along isentropic surfaces with velocity $\mathbf{V}_b$ and the fact that the bounding isentropic surfaces are at fixed positions in isentropic coordinates, the time derivative can be taken outside the volume integral in (9) using the Leibniz rule for differentiation of an integral, to give an evolution equation for Kelvin's circulation, C, in the presence of non-conservative processes:

$$\frac{d}{dt} (C \Delta \theta) = \frac{d}{dt} \int \iint rP \, dA \, d\theta = - \int \oint \left\{ rP (\mathbf{V} - \mathbf{V}_b) + \hat{\mathbf{J}} \right\} . \mathbf{l} \, dl \, d\theta \tag{10}$$

Here, $\Delta \theta$ denotes the separation of the top and bottom boundaries of the volume in isentropic coordinates and C represents the circulation around the lateral boundary averaged over the isentropic surfaces within the layer. If the volume is defined such that the lateral boundary moves with the fluid along the isentropic layer, so that $\mathbf{V}_b = \mathbf{V}$, then circulation must be conserved if the integral of the normal component of non-advective PV flux ($\hat{\mathbf{J}}$) around the lateral boundary is zero, even if diabatic and frictional processes are acting within the volume. A similar integral of the mass continuity equation in isentropic coordinates gives the evolution of volume mass, $\mathcal{M}$:

$$\frac{d}{dt} (\mathcal{M}) = \frac{d}{dt} \int \iint r \, dA \, d\theta = - \int \oint r (\mathbf{V} - \mathbf{V}_b) . \mathbf{l} \, dl \, d\theta - \iint [rQ]_{\text{bot}}^{\text{top}} \, dA \tag{11}$$

Note that the mass of the control volume can change through diabatic heating on the top and bottom faces which enables air to cross these interfaces, while a consequence of the PV impermeability theorem is that there is precisely zero PV flux across these faces.
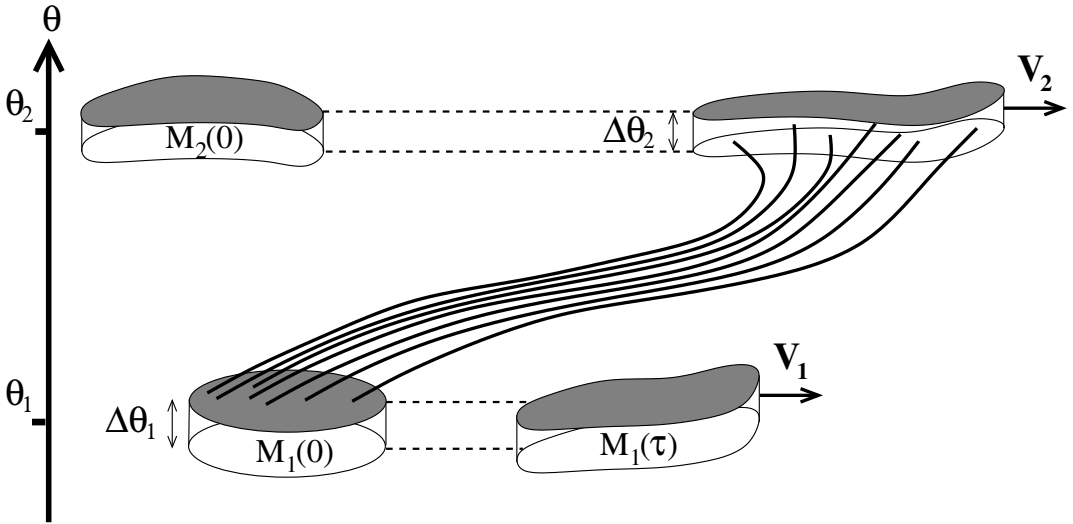
FIGURE 1 Schematic relating the inflow and outflow volumes of a warm conveyor belt (WCB) in the thought experiment of Methven (2015). The inflow volume encompasses the WCB inflow at the initial time, centred on isentropic surface θ_1 with depth $\Delta\theta_1$ and initial mass $M_1(0)$. The lateral boundary of the "inflow volume" follows the horizontal flow within its isentropic layer, velocity $\mathbf{V}_1$, and loses mass through diabatic transport out of its top face, resulting in the inflow volume having mass $M_1(\tau)$ by time $t = \tau$. The coherent ensemble of trajectories (CET) depicts the mass transport in the warm conveyor belt crossing from the inflow volume to the higher outflow volume (centred on θ_2). The CET envelope forms a material volume following the resolved 3-D flow. The outflow volume is defined such that it encompasses the WCB outflow at $t = \tau$. The lateral boundary of the "outflow volume" follows the horizontal flow within its isentropic layer, velocity $\mathbf{V}_2$, and M_2 increases through diabatic mass transport across the bottom face.

2.2 | Conceptual model for WCB inflow and outflow

Methven (2015) introduced a conceptual model of WCBs which was designed to address the question of how latent heating within a WCB affects the negative PV anomaly of the outflow, and therefore subsequent large-scale dynamics in the troposphere and lower stratosphere. It uses a construction that centres on the notion of a WCB "outflow volume" and "inflow volume". Each of these volumes is defined in the same way as the *control volume* of Section 2.1 where the top and bottom faces are isentropic surfaces and the lateral boundary has the same horizontal projection on all isentropic surfaces within the volume. Figure 1 shows how these two volumes are related. The "outflow volume" is defined such that it encloses all the air that is transported diabatically from lower levels in the WCB (depicted by the trajectories in bold lines) in addition to air that follows an almost adiabatic pathway moving within the isentropic control volume. It is assumed that the isentropic layer containing the outflow, $\Delta\theta_2$, is relatively shallow and is no deeper than the net diabatic heating in the WCB which determines the separation between the centre of the outflow, θ_2, and centre of the inflow, θ_1. The climatology of Madonna et al. (2014) supports this hypothesis since in the WCB composites shown it is found that $\theta_2 - \theta_1 \approx 20 - 25K$ and $\Delta\theta_2 \approx 10 - 15K$. An outflow reference time is defined, τ, when the majority of WCB ascent has finished and the mass of the outflow volume at this time is denoted, $M_2(\tau)$.

A key property of the control volumes is that the evolution equations for circulation (10) and mass (11) are derived assuming that the upper and lower isentropic boundaries are invariant and the lateral boundary moves with the horizontal velocity in the isentropic layer (an average over θ at every point around the circuit). So, as the outflow volume

is followed backwards in time it is constrained to remain within the same isentropic layer and distort with the isentropic relative motion. If the lateral boundary can be defined such that it encloses the WCB heating at all times, then (10) shows that the circulation C_2 must be conserved.

However, the mass of the outflow volume clearly must increase as the diabatic mass transport in the WCB brings air into the volume from lower isentropic layers. Defining the net diabatic mass transport as ΔM gives a simple equation for the upper volume mass:

$$M_2(\tau) = M_2(0) + \Delta M \tag{12}$$

where $t = 0$ denotes the "inflow time" when ascent in the WCB begins. Note that since air that has experienced diabatic heating within the WCB typically mixes with air that has followed a more adiabatic pathway, the initial mass is non-zero, $M_2(0) > 0$. The mass-weighted average PV of the outflow volume is given by:

$$\langle P \rangle_2 = \frac{C_2 \Delta \theta_2}{M_2} \tag{13}$$

and must decrease from time 0 to τ since the circulation is conserved, $\Delta \theta_2$ is invariant but the mass increases. In the terminology of Haynes and McIntyre (1990), the total PV substance (PVS) of the volume (i.e., $C_2 \Delta \theta_2$) is diluted by air entering the volume from below such that the PV (analogous to the mixing ratio of PVS) decreases. A surprising conclusion is that $\langle P \rangle_2$ does not depend directly on the initial PV values in the inflow of the WCB - a consequence of the PV impermeability theorem.

Why then is it found in the Madonna et al. (2014) climatology that on average the PV of the outflow equals the PV of the inflow? Methven (2015) uses the concept that a WCB is a coherent ensemble of 3-D trajectories (Wernli and Davies, 1997) to hypothesise that an inflow volume can be identified (with depth $\Delta \theta_1$ centred on θ_1) with a lateral boundary that encloses the majority of the CET at time $t = 0$. This enables calculation of the initial inflow mass, $M_1(0)$, and if it is assumed that all the mass leaving by diabatic mass transport in the WCB ends up in the outflow volume then:

$$M_1(\tau) = M_1(0) - \Delta M \tag{14}$$

In this construction the diabatic heating on the top face of the inflow volume (which enables the WCB diabatic mass transport) cannot change the circulation, C_1, but since this layer is, at least partially, in the atmospheric boundary layer, friction is expected to spin-down circulation $C_1(t)$ (in contrast to the outflow volume). A necessary condition for the average PV of the outflow (at final time) to equal the PV of the inflow (at initial time) is:

$$\frac{C_2(\tau)\Delta \theta_2}{M_2(\tau)} = \frac{C_1(0)\Delta \theta_1}{M_1(0)} \tag{15}$$

One key purpose of this paper is to use observed cases to understand the circumstances under which this relation is approximately satisfied. It involves defining outflow and inflow volumes appropriately and explaining why their circulations are related. The theoretical construct above enables us to address and quantify answers to the following questions:

1. What fraction of mass in the WCB outflow volume (at the outflow time) arrived by diabatic mass transport?
2. How well is the circulation of the outflow volume conserved?
3. What is the geometry of the inflow volume (at inflow time) enclosing air that subsequently ascends in the WCB?

TABLE 1 Summary of case studies. The intensive observing period (IOP) in the NAWDEX campaign and corresponding cyclones, as named by the Free University of Berlin for Vladiana and Walpurga, as named by the NAWDEX team for the Stalactite Cyclone and the Frontal-wave Cyclone. The start time for the MetUM forecast used is shown in each case. The lead time at which the outflow is identified and the isentropic surface at the centre of the outflow layer (± 5 K as described in section 4.1).

IOP	Cyclone Name	Forecast start time (t_0)	Outflow time (t_{out})	Lead ($t_{out} - t_0$)	Outflow centre
3	Vladiana	22/09/16 12 UTC	24/09/16 06 UTC	42 h	325 K
5	Walpurga	26/09/16 12 UTC	28/09/16 00 UTC	36 h	330 K
6	Stalactite Cyclone	30/09/16 12 UTC	02/10/16 06 UTC	42 h	315 K
7	Frontal-wave Cyclone	03/10/16 12 UTC	04/10/16 12 UTC	24 h	315 K

4. Under what circumstances does the average PV of the outflow approximately equal the PV of the inflow?
5. If the outflow circulation integral is unchanged by diabatic processes, in what ways can heating in a WCB influence Rossby waves?

3 | METHODOLOGY, DATA AND MODELLING

3.1 | NAWDEX field campaign and case selection

The four cases used here to investigate heating and mass transport in WCBs and their impacts at tropopause level are taken from the period of the North Atlantic Waveguide and Downstream Impacts Experiment (NAWDEX). Schäfler et al. (2018) define the primary hypothesis that the NAWDEX project sought to address: "Diabatic processes have a major influence on the jet stream structure, downstream development of Rossby waves and eventually high impact weather." The mission focused mainly on cases where developing WCBs transported air to high latitudes (50-70°N) in the North Atlantic sector. In these situations WCB outflow reaches tropopause level and typically expands the synoptic scale ridge area. Sánchez et al. (2020) have shown that in most NAWDEX intensive observing periods (IOPs) the ageostrophic horizontal wind attributable to the balanced (semi-geostrophic) response to heating advects the tropopause on the western and northern flanks of ridges, resulting in ridge areal expansion. Therefore, here we focus on the IOPs where this behaviour has already been established, summarised in Table 1.

3.1.1 | IOP3

A typical situation in the mid-Atlantic where a growing baroclinic wave developed a WCB with strong moisture transport angled from southwest to northeast, crossing Ireland and the northern UK on 23 September 2016. During the 22 September 2016, a frontal wave emerged to the north of Newfoundland. This developed into a cyclone propagating eastward along a baroclinic zone and intensified between the 22nd and 23rd, acquiring the name "Vladiana" from the Frei Universität Berlin. Coordinated aircraft flights both above and within the system on 23 September 2016 measured cloud-microphysical parameters on cross-sections through the WCB using both in situ and remote sensing instruments (Schäfler et al., 2018; Oertel et al., 2019). The anticyclonic branch dominated the outflow of this WCB and in the late stages the whole ridge in which the outflow was embedded broke anticyclonically forming a PV dipole over western Europe (Fig. 2a). Oertel et al. (2020) examined simulated PV anomalies in this case associated with large-scale

ascent and embedded convection and showed that the convective heating formed an elongated PV dipole with the negative flank nearest the jet core, as predicted by the theoretical approach in Harvey et al. (2020). Further, they argued that this PV dipole formed a jet streak altering the large-scale ridge development.

3.1.2 | IOP5

The WCB in this case was zonally oriented occurring in conjunction with a weak cyclone - named Walpurga by the Frei Universität Berlin. The jet stream was very strong at this time, following the formation of a jet streak in IOP4 in association with the extratropical transition of tropical storm Karl (Harvey et al., 2020), and the WCB outflow was entirely into the downstream ridge which did not extend as far meridionally as most of NAWDEX cases. However, this WCB had a high impact through sustained heavy precipitation in Norway and has been described as an atmospheric river case due to the importance of the horizontal moisture flux in the WCB impinging on the orography of western Norway. Figure 2b shows the outflow volume at a stage just before the impact on Norway, illustrating that the ridge is wide and the outflow volume is relatively narrow in the meridonal direction.

3.1.3 | IOP6

The WCB in IOP6 developed as an integral part of the "Stalactite Cyclone" - an explosively deepening cyclone, so named due to the very low tropopause that developed in association with the cyclonic Rossby wave breaking at upper levels. Latent heating was intense in this case and in the later stages (Fig. 2c) there is a clear signature of both the cyclonic and anticyclonic branches of the WCB, although dominated by cyclonic over-turning. Maddison et al. (2019) showed that the downstream block onset over Europe was particularly sensitive to the growth of this cyclone and the representation of diabatic processes. Blanchard et al. (2020) have shown using a combination of observations from the SAFIRE Falcon aircraft and mesoscale model simulations that there were 3 distinct types of embedded convection in this case: low level along the cold front, banded along the bent-back front and mid-level convection. Blanchard et al. (2021) have shown that it is the mid-level convection that contributes to the WCB outflow and formation of an elongated PV dipole with negative PV next to the jet that enhances jet shear and maximum speed.

3.1.4 | IOP7

The "Frontal-wave Cyclone" grew rapidly immediately behind the Stalactite Cyclone and was the focus of IOP7. The WCB outflow of this cyclone re-enforced the ridge built during IOP6 which went on to form a large blocking anticyclone over Scandinavia (Maddison et al., 2019). At the stage shown in Fig. 2d the main ascent phase in this WCB has finished and there is a clear signature of both a cyclonic and anticyclonic branch. However, this is before this new ridge merges with the pre-existing ridge from IOP6 as the positive PV filament between them thinned by the straining flow between the two anticyclonic anomalies.

3.2 | Forecasts with the Met Office global model

For each IOP case study described above we use the data from a single forecast covering the cyclone development period, spanning times that will be identified with the beginning of WCB inflow and the end of the primary WCB outflow. The data stems from re-runs of Met Office operational global forecasts using the Met Office Unified Model (MetUM) in the configuration that was operational during NAWDEX. The MetUM uses a global latitude-longitude grid with

horizontal resolution of $0.15625° \times 0.234375°$ and 90 unevenly spaced terrain-following hybrid-height levels. The UM solves the compressible, non-hydrostatic, deep atmosphere equations of motion using a semi-implicit semi-Lagrangian dynamical core (Wood et al., 2014). Physical processes not resolved or not represented by the dynamics are represented by a suite of parametrizations (see Walters et al. (2017) for more details).

3.3 | Trajectories

Air-mass trajectories are calculated offline from 6-hourly wind fields, output from the UM forecasts, using the Lagrangian trajectory tool (LAGRANTO) (Wernli and Davies, 1997; Sprenger and Wernli, 2015). LAGRANTO employs an iterative Euler method to calculate the updated position of the trajectory from the current wind field and the wind field at the following output time. The method sub-steps between two outputs by interpolating the wind fields in time and position. Here, a 30-minute sub-step is used. LAGRANTO can also calculate back trajectories by multiplying the wind fields by -1 and stepping backwards.

Modifications to LAGRANTO have been made to allow it to use an arbitrary vertical coordinate (instead of pressure). This allows us to use the MetUM output on its native hybrid-height levels rather than interpolating to pressure surfaces. The winds output from the MetUM still need to be interpolated to a common position because of the horizontal C-grid staggering and vertical Charney-Phillips staggering. u and v are linearly interpolated to the center of the C grid then linearly interpolated to model θ-levels (meaning the model levels on which the prognostic variable θ_v is stored, as opposed to isentropic surfaces). w is not interpolated as it is stored at centre points on model θ-levels.

Isentropic trajectories are also calculated using LAGRANTO by interpolating the input horizontal wind fields to an isentropic surface and setting the vertical velocity to zero. This way the trajectories are forced to stay on an individual isentropic surface. It is worth noting that this only works because the situation is reasonably close to hydrostatic balance, as discussed in section 2.1 (i.e. Eqn.(9)).

4 | RESULTS

The results of this paper can be described in terms of the schematic Fig 1. Firstly, we identify the volumes, and coherent ensemble of trajectories connecting these volumes, depicted in Fig. 1. Secondly, we use the identified volumes and trajectories to calculate integral properties of these volumes as a function of time. Finally, we use these results to infer the ways in which the heating in WCBs can influence Rossby waves within the constraints of the PV impermeability theorem. In the following sections, we define an inflow time, t_{in}, and and outflow time, t_{out}, which correspond to times 0 and τ respectively in Fig. 1. This notation is intended to improve clarity and avoid confusion with forecast start time, t_0.

4.1 | Defining the outflow volume of WCBs

WCBs are frequently identified with coherent ensembles of trajectories (CETs) calculated using the 3-D wind field resolved by a model. Typically, the CET is distinguished from all other trajectories by checking for a threshold decrease in pressure over 48 hours (Wernli and Davies, 1997; Madonna et al., 2014). Though useful for distinguishing the WCB from other features in the flow, we are interested in the entire air mass of the WCB outflow volume including air masses with weaker ascent. The ascent threshold approach is likely to neglect some air that enters the WCB outflow by diabatic mass transport. Instead, we start by identifying a WCB outflow as a region of upper tropospheric air that has experienced net diabatic heating (cross-isentropic ascent). To identify this region, a tracer of the initial potential

temperature field, θ_{adv}, is advected passively, online in each forecast experiment, using the tracer advection scheme native to the MetUM. The net diabatic heating over the forecast is then calculated as:

$$\Delta\theta = \theta - \theta_{\text{adv}} \tag{16}$$

as in Chagnon et al. (2013) and Martínez-Alvarado et al. (2016).

Figure 2 demonstrates how the field of $\Delta\theta$ is used to identify the WCB outflow. The colour shading in Figure 2 shows the field $\Delta\theta$ on an isentropic surface for each case study. In each case study there is a distinct region with $\Delta\theta > 0$ in the tropospheric air of a ridge. The WCB outflow is distinctive because air which experiences little or no latent heating will typically have $\Delta\theta < 0$ due to the effects of long-wave radiative cooling. Air in the WCB outflow will also experience radiative cooling such that older air in the outflow will have cooled more and have a lower net heating, $\Delta\theta$.

The WCB outflow can be identified by drawing a contour of $\Delta\theta = 0$. However, there is finescale structure in the $\Delta\theta$ field that would render the boundary of the outflow volume too convoluted to follow reliably in the back trajectory calculations that follow. So, before drawing the contour, a moving median filter with a size of 25x25 grid-points has been applied to $\Delta\theta$ to remove small-scale features. This is a smoothing filter, and removes features with a width of less than around 250 km. Different filter sizes were tested and the filter size of 25 was found to adequately smooth $\Delta\theta$ while still encircling the majority of the positive $\Delta\theta$.

Generally, the regions with $\Delta\theta > 0$ in Fig. 2 do not cross the tropopause but the smoothing of the field of $\Delta\theta$ by the median filter can have the undesired effect of causing the zero contour to cross the tropopause (2 PVU contour) and encompass stratospheric air. Therefore, an additional criteria that PV< 2 PVU is also applied to avoid including stratospheric air in the definition of the outflow volume. A median filter with a size of 5x5 gridpoints is applied the PV field prior to applying this criteria. An advantage of the median filter over a Gaussian mean filter or other mean filters is that it better preserves the locations of abrupt changes between regions of different values - typical of the PV field and its abrupt contrast across the tropopause. Therefore, including median-filtered PV retains the sharp tropopause boundary. This does not work so well where there are filaments of high PV which is why we apply the filter with a smaller size for PV than for $\Delta\theta$.

The outflow boundary identification algorithm is run on multiple isentropic surfaces for each case study (300-350 K every 5 K). We select isentropic surfaces as outflow layers where there is a large area of diabatic heating in a ridge. The ridge criteria is to ensure that we are looking at the WCB outflow rather than identifying air masses on lower isentropic surfaces that are still likely to be in the process of ascending. The resulting outflow volume boundary diagnosed from $\Delta\theta > 0$ and PV< 2PVU is shown by the cyan contours in Fig. 2. For each case study we identify three isentropic outflow layers. The isentropic surface shown in Fig. 2 for each case study is in the middle of these chosen isentropic surfaces with the others at ± 5 K. This covers the majority of the outflow in each case. An exception is IOP7 where there are still large regions of diabatically heated air above the chosen outflow layers. These isentropic surfaces were not included here because there was more diabatically heated air to the west of the outflow region associated with a separate WCB and the contouring method could not separate these two outflows.

In each case study there is a "tail" of high $\Delta\theta$ from the southwest corner of the diagnosed outflow that is excluded by the smoothing. This is the part of the WCB where heating is still active above the cold front at the chosen outflow time, t_{out}. This is a limitation: it is generally not possible to identify an outflow time when the heating in the WCB of interest has finished, but another WCB has not started to influence the ridge. For each case study, the outflow identification was run at multiple lead times and the chosen outflow time was taken as the time where the contour appeared most well defined and captured the majority of the WCB outflow (see Bland (2018) for more details). This is a balance between identifying all the WCB mass and having an outflow boundary that can be tracked far enough back in time. Also, since the
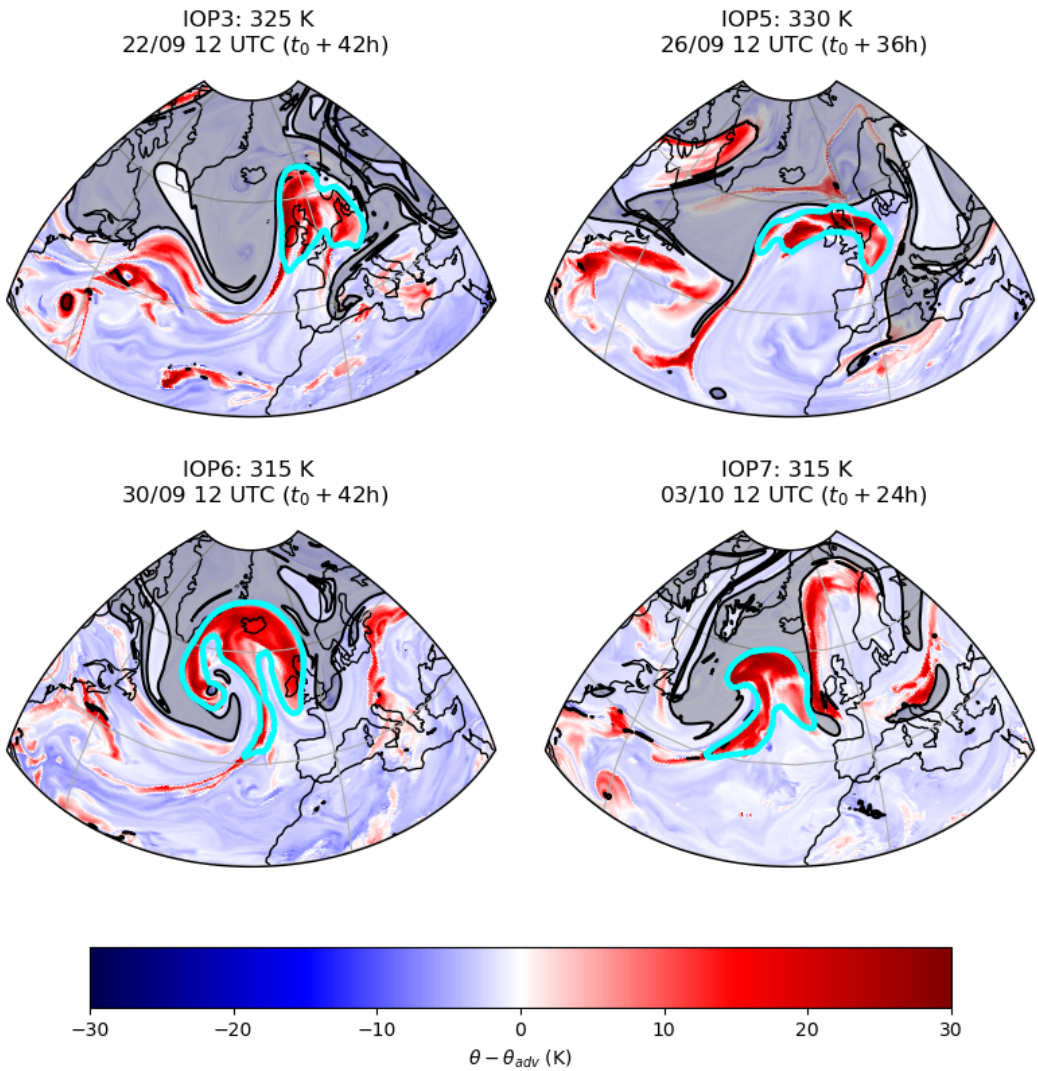
FIGURE 2   Identified outflow region for each case study at the outflow time (see table 1). Colour shading in each figure shows the net diabatic heating of airmasses diagnosed by a tracer of potential temperature ($\Delta\theta = \theta - \theta_{adv}$) ending on an isentropic layer from the corresponding forecast. A contour of PV=2 is overlaid with regions of PV>2 shaded in grey for clarity. The cyan lines show the diagnosed outflow region for the isentropic surface (identified using smoothed fields of $\Delta\theta$ and PV). The limited area of the data is the range of data archived from the MetUM to cover the NAWDEX campaign.
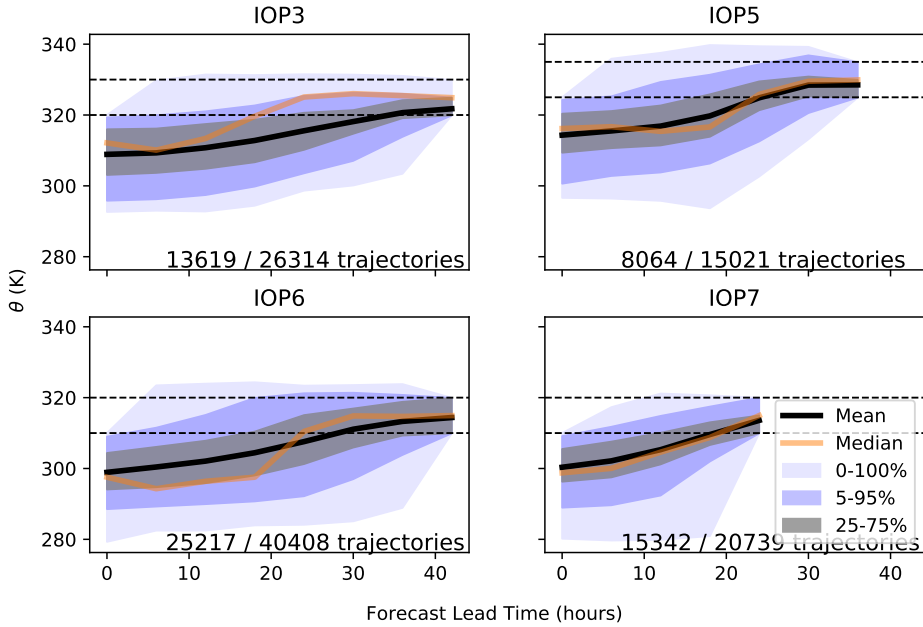
FIGURE 3 The distribution of potential temperature (θ) following 3-D Lagrangian trajectories calculated backwards from the outflow volume diagnosed in each case study. Only trajectories that have a value of θ at the start of the forecast (t_0) that is below the lower boundary of the isentropic outflow layer are included (i.e., the trajectories that ascend diabatically into the outflow). The number of trajectories selected from the total set of trajectories is given in each panel. The "median trajectory" shown for each case is an individual trajectory with the median net change in θ (diabatic heating) from trajectories that ascend into the middle outflow layer.

active "tail" of heating is narrow where it intersects the outflow volume boundary (by definition due to the smoothing approach), it is still expected that its contribution to the boundary integral of the non-advective PV flux (see (10)) up to the outflow time is small, and elsewhere heating on the boundary is zero, and therefore that the circulation of the outflow volume is approximately conserved.

4.2 | Tracing the outflow backwards in time

There are two parts of the outflow that we want to trace: the diabatic mass transport into the outflow by the WCB, indicated by the coherent ensemble of 3-D trajectories in Fig. 1 that originate in the inflow, and the history of isentropic motion of the outflow volume (the adiabatic pathway). To trace back the path of the WCB, 3-D back trajectories are calculated from every MetUM grid point within the lateral boundary of the outflow on each isentropic surface. We select the subset of these 3-D trajectories that also originate below the lower bounding surface of the outflow layer as "WCB trajectories":

$$\theta_{\text{traj}}(t_0) < \theta_2 - \frac{1}{2}\Delta\theta_2, \tag{17}$$

where t_0 is the forecast start time. θ_2 is the centre of the outflow volume and $\Delta\theta_2$ is the depth of the outflow volume following Fig. 1.

Figure 3 shows the distribution of θ for the WCB trajectories. The WCB trajectories show steady diabatic heating over the course of the WCB with an average diabatic heating of $\approx 10 - 15$ K. This is lower than the 20 K found by Madonna et al. (2014) but we would expect the average to be lower since we are considering all the airmasses that ascend diabatically into the outflow rather than those with net ascent above a threshold. For the same reason, we also see that the initial points of the WCB trajectories are spread over a larger vertical extent here. However, we also can not rule out that some of the WCB ascent has occurred prior to the start of the forecast. We are looking at a shorter time period than the usual 48h used to detect WCBs from trajectories and in all cases, except IOP3, the distribution of θ is increasing from the start of the forecast. The distribution of θ increasing implies diabatic heating and ascent occurring in the WCB and may be occurring prior to the forecast start time.

To trace the isentropic motion of the outflow volume, isentropic back trajectories are calculated from the same gridpoints as the 3-D trajectories. By definition, all the of isentropic back trajectories must remain within the boundary of the control volume constrained to the isentropic layer $\theta_2 \pm \frac{1}{2}\Delta\theta_2$, as depicted in Fig. 1. In contrast, θ will change along the 3-D back trajectories, reflecting diabatic heating or cooling. If each 3-D trajectory is compared with an isentropic back trajectory from the same grid-point, the horizontal projection of their paths will also differ as the 3-D trajectory moves to different isentropic surfaces, given that there is shear in the horizontal wind between the isentropic surfaces.

Figure 4 shows the horizontal displacement of 3-D back trajectories relative to their corresponding isentropic back trajectories versus displacement in θ below the outflow. In all cases, the maximum trajectory number density in the plots is near the origin, corresponding to 3-D back trajectories that are approximately adiabatic ($\Delta\theta \approx 0$) and therefore can have little horizontal displacement relative to the isentropic trajectories. However, the 3-D trajectories that experience heating show horizontal displacements that are correlated with the net heating. There is strong variation between cases, with the least horizontal displacement in IOP5 that was characterised by strong zonal flow and a broad, large-scale ridge, and most displacement in IOP7, characterised by a rapidly developing cyclone with the strongest heating on average. The implication is that the baroclinic shear across isentropic surfaces intersected by the WCB is weak in the weak cyclone development case IOP5, and strong in IOP7 where baroclinic growth is fastest.

Another branch of trajectories, with relatively small population within the outflow volumes defined, is distinguished by 3-D trajectories originating much further west and experiencing weak cooling. Examination reveals that these trajectories travel close to the core of the jet stream, experiencing radiative cooling. Although the cooling is weak, the wind shear is strong immediately below the jet core. It is found that the 3-D trajectories originate further away than the corresponding isentropic trajectories because they begin in the jet core and descend slowly out of it en route to the outflow volume.

4.3 | Defining the WCB inflow volume

An inflow volume is sought that at an earlier "inflow time", t_{in}, contains the majority 3-D trajectories associated with the WCB, as depicted in Fig. 1. The inflow time is identified with the time when substantive heating begins along the 3-D trajectories associated with the WCB (Fig. 3); however, as discussed in section 4.1, the WCB heating is already active from the start of the forecast in most of the cases. Therefore, the inflow time used in Fig. 3 is the same as the forecast start time, t_0, although the inflow time definition will be refined later.

To define the inflow volume, we first select the subset of 3-D trajectories that meet the criterion for "WCB trajectories" (17); therefore the same trajectories as shown in Fig. 3. The inflow volume is then defined as the lateral boundary enclosing the horizontal projection of all these WCB trajectory points at the inflow time and is shown by the
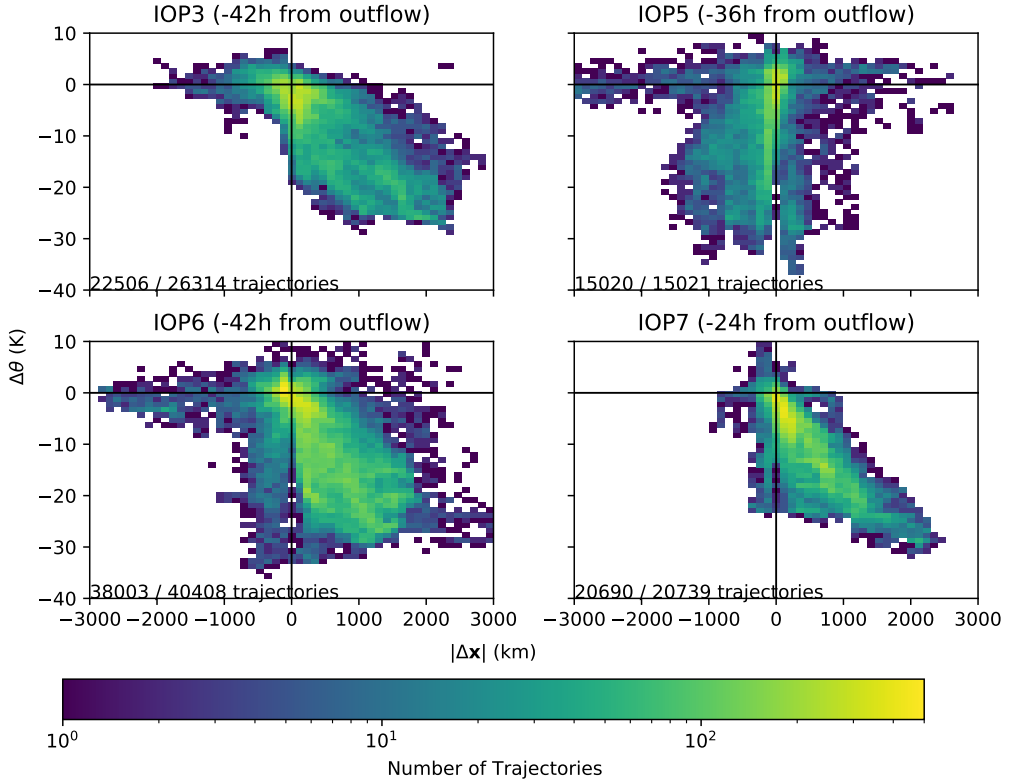
FIGURE 4 The difference in θ and horizontal position ($|\Delta\mathbf{x}| = r \cdot \sqrt{(\cos(\phi)\Delta\lambda)^2 + (\Delta\phi)^2}$) between the 3-D trajectories and the corresponding isentropic back trajectories released from matching coordinates in the outflow volume at the outflow time (t_{out}). Differences are shown for trajectories tracked back to the forecast start time, t_0. In contrast to Fig. 3, all trajectories are shown not just trajectories that experience net heating; however, some of the isentropic trajectories move out of the data domain so are not included. The number of trajectories selected out of the total set is given in each panel. The difference in horizontal position is multiplied by the sign of the displacement in longitude to distinguish air masses that start east of the outflow volume ($|\Delta\mathbf{x}| > 0$) or west of the outflow volume ($|\Delta\mathbf{x}| < 0$). $\Delta\theta < 0$ here implies that the trajectories originate at lower θ than the outflow.

magenta curve in Fig. 5.

The cyan curve in Fig. 5 shows the outflow (upper isentropic) volume at the inflow time. The outflow volume shown is derived by drawing a lateral boundary enclosing the horizontal projection of the isentropic back trajectories originating from all gridpoints within the outflow volume at the outflow time. A remarkable finding is that the inflow volume defined using the 3-D WCB trajectories is mostly over-lapping with the footprint of the outflow volume (at inflow time) identified using isentropic trajectories. However, there is a clear shift in the inflow boundary relative to the outflow volume boundary, especially in IOP6 and IOP7, where the outflow volume at the inflow time is further upstream than the locus of the inflow volume. This behaviour was anticipated by Methven (2015) in Fig. 1 due to wind speed generally increasing with height beneath the jet stream core.

The overlap of the inflow and outflow volumes at the inflow time may also be exaggerated by treating trajectories with relatively small ascent as part of the inflow. The dashed magenta line in Fig. 5 shows the inflow volume boundary found if we only select trajectories that start at least 10 K below the lower boundary of the outflow volume. This sub-selection of inflow trajectories has a more pronounced shift relative to the outflow boundary which decreases the overlap in IOP6 and IOP7. However, in IOP3 and IOP5 the overlap of the inflow volume with the outflow volume is largely unchanged.

In summary, it is possible, in the diverse WCB cases examined, to identify an "inflow volume" possessing a coherent lateral boundary at the inflow time. However, the inflow layer defined here can span all isentropic surfaces below the outflow layer. Surprisingly, given the strong shear environment at the cold front associated with each WCB, the lateral boundary of the inflow volume at inflow time is quite similar to the lateral boundary of the outflow volume at the same time. One plausible explanation is that air in the WCB "slides" up the frontal surface as it experiences condensation and latent heating associated with ascent. While there is strong shear across the sloping frontal surface, WCB trajectories do not cross the frontal surface and so the difference in horizontal winds between the WCB inflow and outflow is much smaller than the cross-frontal shear. For example, see the frontal cross-section and set of WCB trajectories points shown in Martínez-Alvarado et al. (2014).

4.4 | Integral properties of the WCB outflow volume

In this section the integral properties of the WCB outflow are calculated. To trace the boundaries of the isentropic outflow volume, isentropic back trajectories are calculated from nodes along the outflow boundary contour on each isentropic surface, together tracing the circuit backwards in time. The circulation of the outflow volume is calculated first using horizontal wind data at the nodes forming the discrete representation of the boundary of the outflow volume. Since these nodes are also used as the departure points for the isentropic back trajectories, the same method can be used to calculate circulation at any time from the forecast start time, $t = t_0$, to the outflow time, t_{out}. Kelvin's circulation integral is defined by:

$$C = \oint \mathbf{u}_{abs} \cdot \mathbf{dl}, \tag{18}$$

which we can calculate as a circuit integral around the outflow boundary on each isentropic surface. In detail, the circulation is calculated from the position and velocity in spherical coordinates (longitude, λ; latitude, ϕ) using a trapezoidal method to represent the line integral by sum over nodes (index j):

$$C \approx \sum_j \quad u_j \cdot (a + z_j) \cdot \cos\phi_j \cdot \frac{1}{2}(\lambda_{j+1} - \lambda_{j-1}) + v_j \cdot (a + z_j) \cdot \frac{1}{2}(\phi_{j+1} - \phi_{j-1}) + w_j \cdot \frac{1}{2}(z_{j+1} - z_{j-1}) \tag{19}$$
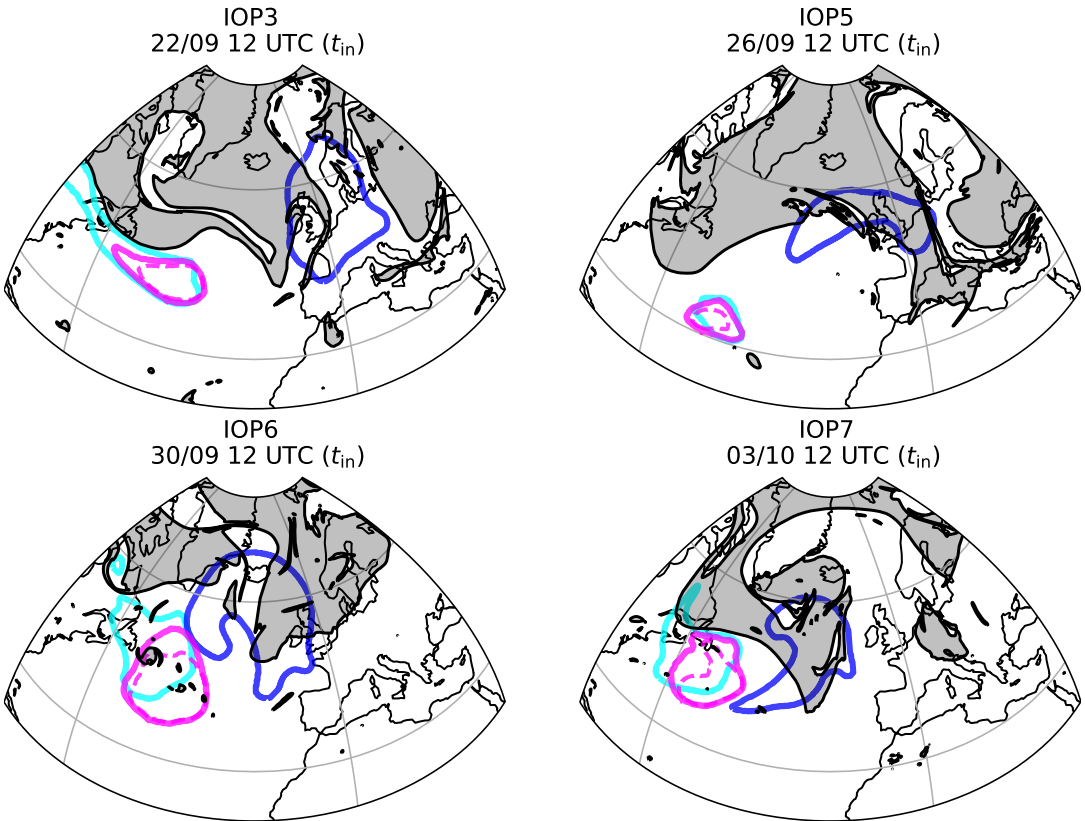
FIGURE 5 Depicting the inflow and outflow volumes associated with the WCB cases. The solid magenta contour is the lateral boundary of the "inflow volume" at inflow time, t_{in} (corresponding to the bottom-left volume in Fig 1) which encompasses the origins of the 3-D WCB trajectories traced backwards from grid-points within the outflow volume. The dashed magenta contour shows the inflow volume (at inflow time) calculated for a subset of these trajectories are at least 10 K lower than the bottom boundary of the outflow volume. The blue contour shows the "outflow volume" at the outflow time, as in Fig. 5 (corresponding to the top-right volume in Fig 1) and the solid cyan contour is the outflow volume at the inflow time (corresponding to the top-left volume in Fig 1). Note that some of the isentropic trajectories are out of bounds at the inflow time in IOP3 and IOP6, cutting the boundary off at the western edge of the domain.

The inclusion of the vertical velocity w and the addition of the altitude to the earth's radius in $(a + z_j)$ in these calculations are consistent with the MetUM being a non-hydrostatic, deep-atmosphere model. The calculation of line integrals allows us to consider the separate contributions from the relative velocity ($\mathbf{u}_{rel} = (u, v, w)$) and the planetary velocity $\mathbf{u}_{rot} = (\Omega \cdot (a + z) \cos \phi, 0, 0)$ to the total circulation (note that $\mathbf{u}_{abs} = \mathbf{u}_{rot} + \mathbf{u}_{rel}$).

The circulation can also be calculated from an area integral of vorticity ζ_θ defined from Ertel PV using (7). This is achieved by calculating the area, at each grid box, index i:

$$A_i = \sum_i (a + z_i)^2 \cdot \cos \phi_i \cdot d\lambda \, d\phi \tag{20}$$

then the volume, $V_i = A_i \, \delta z_i$ where δz_i is computed as the difference between the geopotential height on isentropic surfaces $\theta_i \pm \frac{\delta \theta}{2}$. This allows use to calculate the mass (M_i) and circulation (C_i) of the grid box as:

$$M_i = \rho_i V_i, \qquad C_i = \frac{M_i P_i}{\delta \theta}, \tag{21}$$

The integral of each of these quantities can then be calculated as the sum over all grid-boxes bounded by the outflow boundary. Note that we do not account for the fraction of box area within the bounding circuit: a grid-box contributes to the area integral if its centre point is within the circuit.

Figure 6 shows the circulation (comparing both calculation methods) and mass as a function of time for the outflow volume in each case study. The outflow time, t_{out}, is marked by the vertical line. The curves stop once the outflow boundary on an isentropic surface crosses out of the data domain (following isentropic trajectories backwards or forwards). As theorised, the circulation line integral is approximately conserved during the WCB ascent period ($t < t_{out}$ while M_2 is increasing) with a fractional variation with time of less than 15%. In contrast, the mass increases markedly, by as much as 80%, through diabatic mass transport from below. There is some disagreement in circulation estimates at early times before the mass increase in the outflow layer starts in IOP5 and IOP6. This inconsistency is attributed to the volume becoming very long and narrow and sometimes folded, and therefore the numerical integrals become inaccurate due to the limitations of tracking the circuit using offline back trajectories with 6-hourly wind data.

Changes in the outflow integrals are therefore followed from the "initial ascent time",

$$t_a = t_{out} - \Delta t, \tag{22}$$

when the outflow mass first increases (and circulation integrals are consistent). The values of Δt are shown in Table 2. The circulation integrals on the top isentropic surface for IOP3 do not agree at any time so the time, t_a, is only defined by the mass increasing. This is due to small-scale noise in PV and overturning isentropic surfaces associated with partially resolved gravity wave breaking in the model on this layer and above. Similar noise in PV can be seen at tropopause level above the WCB outflow in the Meso-NH simulations of IOP6 (Blanchard et al., 2021).

In some cases, particularly IOP7, the mass of the outflow volume continues to increase after the outflow time. This is due to diabatic mass transport indicating that the WCB is still active. An outflow volume could be defined at a later time that encloses this extra diabatic mass transport but we have to balance this consideration with being able to track the outflow volume backwards in time. Although this highlights the difficulty in defining a fixed outflow time for a WCB, it is unimportant for the results shown here. The important result is that the circulation is approximately conserved in the outflow volume up to the selected outflow time. An outflow volume could still be defined at a later time with a larger area to encompass this additional diabatic mass transport. However, since there are limitations in how long we can track these volumes, the outflow time is defined at a time when we can capture the majority of the diabatic mass
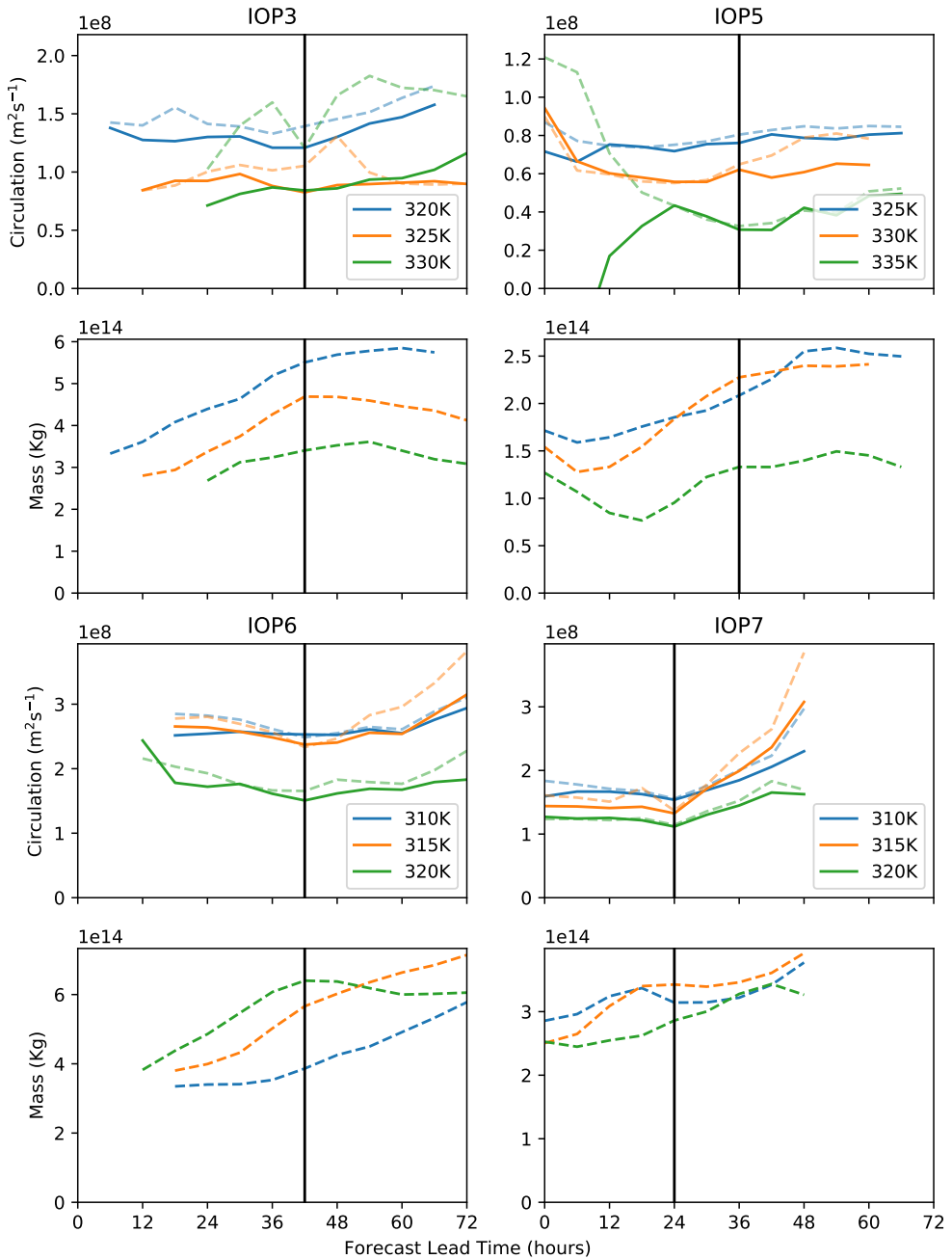
FIGURE 6 Circulation and mass of the outflow volume as a function of time for each case study. The solid lines show circulation calculated using a line integral around the isentropic trajectories initialised on the boundary of the outflow. The dashed lines show circulation (and mass) calculated using integrals over the area enclosed by the isentropic trajectories (assuming a ±1 K spacing in height to calculate the mass). The vertical line shows the outflow time, t_{out}, for each case study; the WCB is active before this time.

transport associated with the WCB and the volume is not too convoluted through advection.

Figure 7 shows the bulk properties of the WCB outflow defined by mass-weighted averages. The average isentropic density, PV, absolute and relative vorticity are calculated as follows:

$$\langle r \rangle_2 = \frac{\mathcal{M}_2}{A_2 \Delta \theta_2} \; ; \quad \langle P \rangle_2 = \frac{C_2 \Delta \theta_2}{\mathcal{M}_2} \; ; \quad \langle \zeta \rangle_2 = \frac{C_2}{A_2} \; ; \quad \langle \xi \rangle_2 = \langle \zeta \rangle_2 - \langle f \rangle_2 \tag{23}$$

where $\langle f \rangle_2$ stands for the Coriolis parameter averaged over the area of the outflow. The incoming diabatic mass flux contributes to both an increase in isentropic density (reduction in static stability) and also an increase in outflow area associated with horizontal divergence:

$$\frac{\Delta \mathcal{M}}{\mathcal{M}_a} = \frac{\Delta r}{\langle r \rangle_a} + \frac{\Delta A}{A_a} \tag{24}$$

Here the increases are described as fractional increases relative to values at the earlier "ascent time", $t_a = t_{out} - \Delta t$. This corresponds to the time when the outflow mass, M_2, starts increasing (and circulation estimates are consistent). Circulation conservation also implies that:

$$\frac{\Delta \zeta}{\langle \zeta \rangle_a} = -\frac{\Delta A}{A_a} \tag{25}$$

so that absolute vorticity must decrease as outflow area increases. This also implies that the relative vorticity of the outflow volume must become more negative (anticyclonic). From (24) alone it is not possible to determine the partition of the mass increase between increasing density and area. However, from the PV definition (8) it is possible to express the fractional PV anomaly associated with the diabatic mass flux as a partition between vorticity and density anomalies:

$$\frac{\Delta P}{\langle P \rangle_a} = \frac{\Delta \zeta}{\langle \zeta \rangle_a} - \frac{\Delta r}{\langle r \rangle_a} = -\frac{\Delta \mathcal{M}}{\mathcal{M}_a} \tag{26}$$

The insight into balance associated with PV invertibility that comes from quasi-geostrophic theory then indicates that there is approximate equipartition between the vorticity and stratification (or isentropic density) anomalies in the situation when the PV anomaly is approximately isotropic in 3-D (and the height axis is re-scaled by N/f). When the PV anomaly is shallower then there is more amplitude in the stratification anomaly; when it is deeper then is more amplitude in vorticity. Substituting (25) into (26) it is then immediately clear that PV inversion also determines the partition of the diabatic mass increase between density increase and fractional area increase.

Table 2 summarises the relative change in integral properties of the outflow volume for each case study during the time window $t_a \leq t \leq t_{out}$. The change in mass is much greater than the magnitude of change in circulation, except for the top isentropic layers in all IOPs where the circulation changes have greater magnitude (although still smaller than mass increase) and can also be quite inconsistent between the contour integral and area integral estimates (related to small scale noise in model PV on these higher levels just beneath the tropopause, as explained above).

In the cases examined, the fractional area increase is considerably greater than the isentropic density increase. Although the circulation integral for the outflow volume is approximately unchanged by the WCB heating, there are still three major influences of the diabatic mass transport:

1. Outflow area increases as a result of horizontal divergence; the result is that the larger the area becomes the greater its anticyclonic flow anomaly as measured by average relative vorticity.
2. Diabatic mass transport enables air to cross to higher isentropic surfaces. The increased altitude of the low PV air
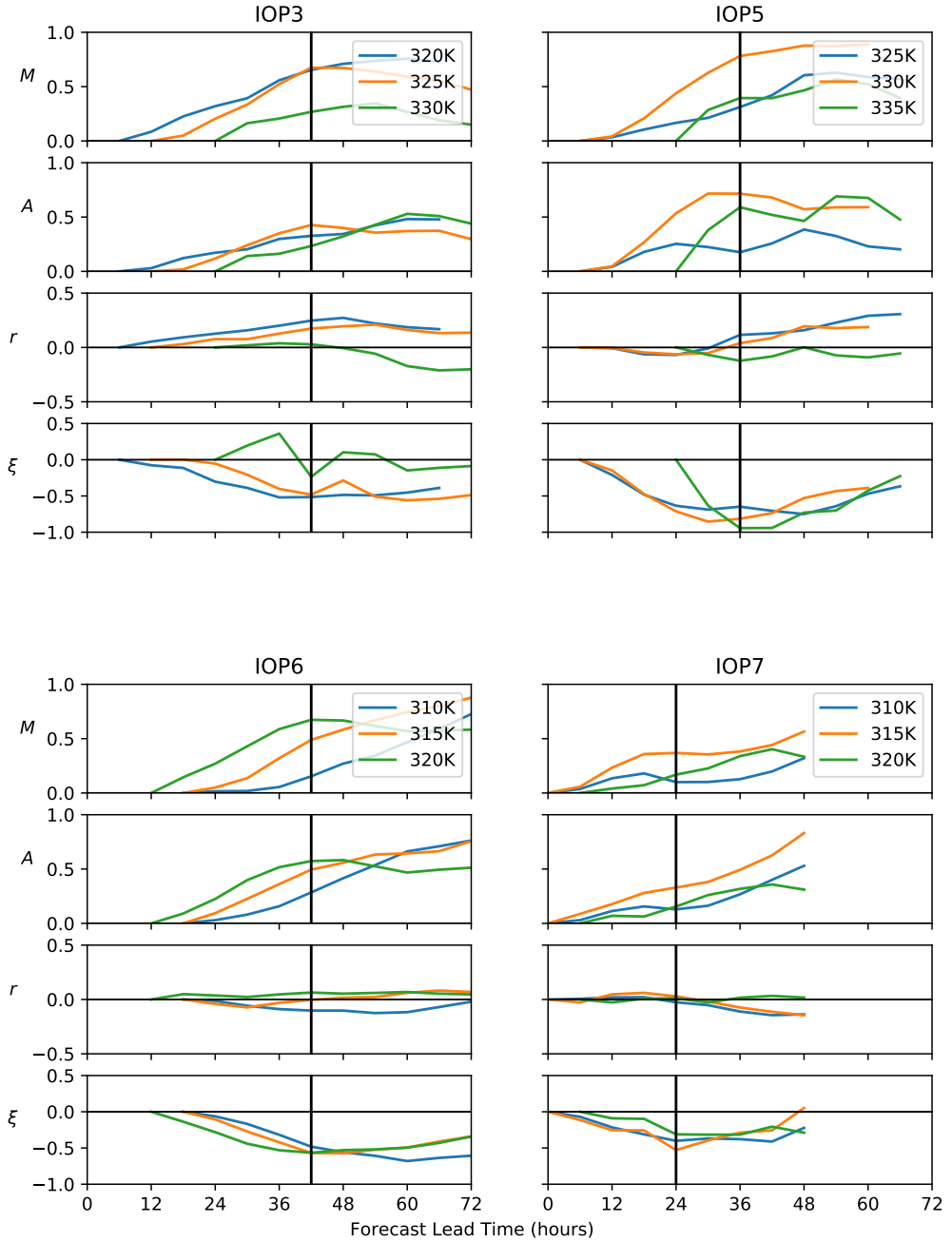
FIGURE 7 Time series of WCB outflow mass (M), area (A), average isentropic pseudo density (r), and relative vorticity (ξ). Shown as a fractional change relative to an earlier ascent time, $t_a = t_{out} - \Delta t$ with the anomaly of relative vorticity (ξ) shown relative to the absolute vorticity (ζ) at t_a. The value of Δt used for each case and outflow level is shown in Table 2. The vertical line shows outflow time, t_{out}, for each case study.

TABLE 2 The percentage change in circulation (C), mass (M), area (A), absolute vorticity (ζ), planetary vorticity (f), and relative vorticity (ξ) of the outflow volume across the four considered cases. Changes are given as a percentage change relative to the value at an earlier ascent time, $t_a = t_{out} - \Delta t$. θ is the isentropic surface considered in Kelvin. The change in circulation shown is that calculated from the line integrals with the circulation from the area integrals in brackets. Note that the change in the relative and planetary vorticity is shown relative to the absolute vorticity, ζ, at time t_a.

Case	Δt (hr)	θ (K)	$\frac{\Delta C}{C(t_a)}$	$\frac{\Delta M}{M(t_a)}$	$\frac{\Delta A}{A(t_a)}$	$\frac{\Delta \zeta}{\zeta(t_a)}$	$\frac{\Delta f}{\zeta(t_a)}$	$\frac{\Delta \xi}{\zeta(t_a)}$
IOP3	36h	320	-12.3 (-2.2)	65.4	32.7	-26.3	23.6	-49.9
	30h	325	-2.2 (25.0)	67.4	42.7	-12.4	35.9	-48.3
	18h	330	18.1 (17.7)	26.8	23.3	-4.6	11.8	-16.3
IOP5	30h	325	14.8 (4.2)	31.2	17.6	-11.4	44.2	-55.6
	30h	330	-6.6 (5.2)	78.2	71.5	-38.7	49.2	-87.9
	12h	335	-29.1 (-24.7)	39.5	59.0	-52.6	42.0	-94.6
IOP6	24h	310	0.6 (-12.8)	15.4	28.5	-32.1	10.4	-42.5
	24h	315	-10.6 (-16.0)	48.9	49.5	-43.8	10.5	-54.3
	30h	320	-38.2 (-23.4)	67.3	57.3	-51.3	12.6	-63.9
IOP7	24h	310	-3.4 (-15.2)	10.0	12.9	-24.9	9.9	-34.8
	24h	315	-8.0 (-15.0)	36.8	33.0	-36.0	11.3	-47.4
	18h	320	-10.1 (-7.6)	16.9	15.5	-20.0	11.4	-31.4

makes it more anomalously negative in PV relative to air elsewhere at the same latitude and altitude.

3. On the higher isentropic surfaces reached due to heating, the Rossby wave breaking behaviour is different - typically the anticyclonic branch becomes stronger relative to the cyclonic branch of the WCB on higher surfaces.

Note that the relative vorticity becomes more negative as a result of both the area increase of the outflow volume and the adiabatic change arising from the poleward displacement of the whole circuit, such that the average Coriolis parameter within the circuit increases and the relative vorticity decreases by a corresponding amount. In this way, the roles of meridional advection and divergent outflow in the anomalous vorticity pattern of a Rossby wave are apparent. By comparing the $\Delta \zeta$ and Δf columns of Table 2, it can be seen that the "area expansion" and "poleward displacement" contributions to the anticyclonic relative vorticity anomaly are similar in magnitude. The adiabatic contribution from poleward displacement is greater in IOP3 while the area expansion contribution is greater in IOP6 and IOP7. The total relative vorticity contribution is large, reaching almost 100% of the initial absolute vorticity of the control volume in IOP5.

4.5 | Relating PV of the WCB outflow to the inflow

The fourth question posed in Section 2 is why it is found in composites of many cases that the average PV of the WCB outflow is approximately equal to the PV of the inflow (Madonna et al., 2014). This amounts to explaining why (15) holds. The first step is to explain why the circulation of the inflow volume might be related to the circulation of the outflow. A key finding is that, at the inflow time, the lateral boundaries of the outflow volume (traced backwards using isentropic

trajectories) and the WCB inflow volume (defined using 3-D back trajectories from the outflow volume) are similar so that there is large overlap in the horizontal projection of both volumes (Fig. 5). Circulation is defined by the circuit integral of velocity around these boundaries. Since the two circuits are similar at the inflow time and move similarly over the next few hours, it is plausible that the velocities on the two circuits are sufficiently similar that the circulation integrals at inflow time are approximately equal:

$$C_1(t_{\text{in}}) \approx C_2(t_{\text{in}}) = C_2(t_{\text{out}}) \tag{27}$$

A caveat to this conclusion is that the circulation is the integral of the tangential component of velocity at every point around the circuit, while this component cannot move the circuit. So it would be possible in principal to construct a flow where the circulations differ even though the circuits move together. However, since the large-scale flow is dominated by its non-divergent component this is unlikely. Note that the last step in (27) comes from the conservation of circulation for the outflow volume, which has been demonstrated to hold to a good approximation using the data (Fig. 6). Therefore, the circulation terms on both sides of (15) are approximately equal, reducing the equation to:

$$\frac{\mathcal{M}_2(t_{\text{out}})}{\Delta\theta_2} \approx \frac{\mathcal{M}_1(t_{\text{in}})}{\Delta\theta_1} \tag{28}$$

$$\langle r \rangle_2 (t_{\text{out}}) A_2(t_{\text{out}}) \approx \langle r \rangle_1 (t_{\text{in}}) A_1(t_{\text{in}}) \tag{29}$$

Note that the second form of this equation comes directly from the definition of average isentropic density. No knowledge is required on the final state of the inflow volume. Although it was argued above that $A_1(t_{\text{in}}) \approx A_2(t_{\text{in}})$, there is no clear relation to $A_2(t_{\text{out}})$ other than it is expected that $A_2(t_{\text{out}}) > A_2(t_{\text{in}})$. Also, there is not a clear relation between the densities other than the climatological expectation that isentropic density is greater in the lower troposphere, $\langle r \rangle_1 > \langle r \rangle_2$ (at any time).

Now examining the NAWDEX cases, Figure 8 shows the average PV calculated in evenly spaced isentropic layers bounded by the lateral contour of the outflow volumes (cyan symbols) and the inflow volumes (magenta symbols). The inflow volume PV increases as a result of diabatic mass flux out of the volume and the concentration of PV substance. In contrast, the outflow volume PV decreases from the time $t_a = t_{\text{out}} - \Delta t$, when the WCB outflow mass increase begins, to the outflow time, t_{out}, as a result of dilution of PV substance. Note that the outflow is not followed to times earlier than t_a because of numerical issues in calculating the circulation at earlier times and the outflow volume also leaves the data domain in some IOPs. In IOP5 and IOP7 it is the case that the PV of the outflow at t_{out} is approximately equal to the PV of the inflow layers at t_{in}, especially those that subsequently experience the greatest diabatic mass flux divergence and PV concentration. In IOP3 and IOP6 the PV of the outflow at final time, in all layers, is distinctly lower than the PV of all inflow layers.

Returning to (28) it is found in the climatological WCB composites of Madonna et al. (2014) that $\Delta\theta_2 \le (\theta_2 - \theta_1)$. Therefore, if the top of the inflow adjoins the bottom of the outflow layers, at $\theta_2 - \frac{1}{2}\Delta\theta_2$, it is reasonable to suppose that $\Delta\theta_1 \approx \Delta\theta_2$. If this is the case then (28) holds if the mass of the outflow (at outflow time) equals the mass of the inflow (at inflow time), i.e., $\mathcal{M}_2(t_{\text{out}}) = \mathcal{M}_1(t_{\text{in}})$. The finding from the NAWDEX case studies is that the circulation of the upper-level outflow volume is indeed conserved in the presence of the WCB heating but that consistent outflow and inflow volumes can be defined meeting the specifications of (28) only in some cases. In the WCB cases with the strongest diabatic mass transport (IOP3 and IOP6) the outflow is still relatively shallow, but with a large influx of mass from lower isentropic layers, giving rise to larger $\mathcal{M}/\Delta\theta$ than the inflow volume (encompassing the layers that the WCB trajectories originate from at the inflow time). The consequence is that the average PV of the outflow ends up smaller than that of the inflow (at t_{in}) in these cases.
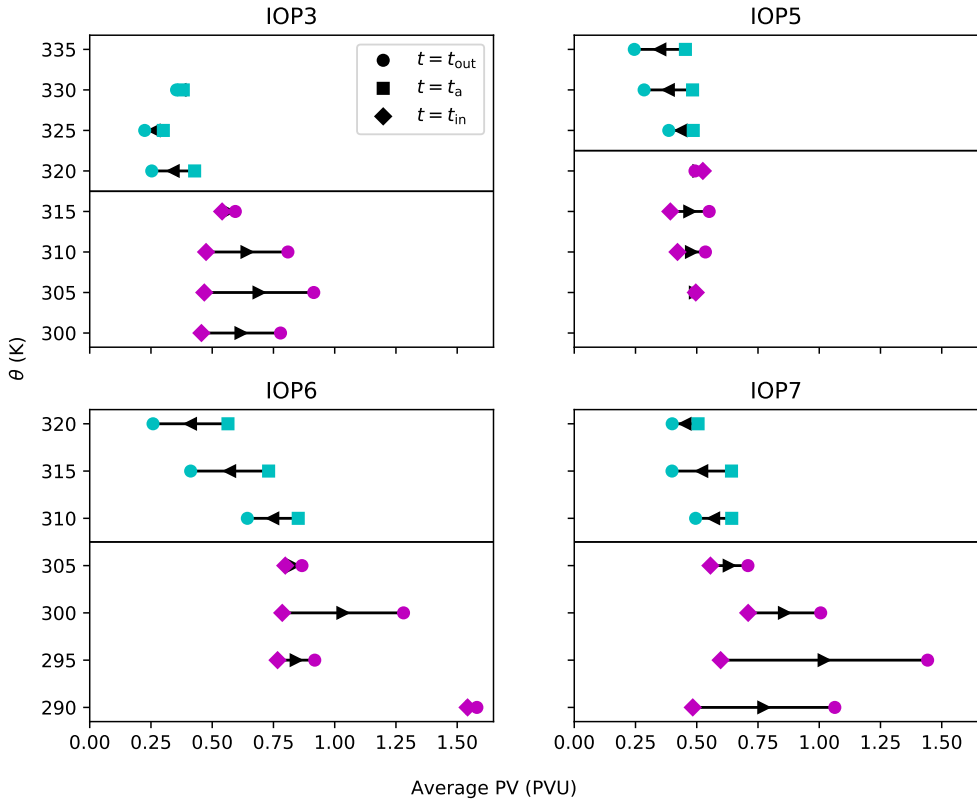
FIGURE 8 The average PV of the outflow (cyan) and inflow (magenta) volumes for each case study. The arrows show the change in PV leading up to the outflow time (Fig.2). Note that the outflow volumes are traced back to the "initial ascent time", $t_a = t_{out} - \Delta t$, when outflow mass begins to increase, where Δt is given in Table 2. The inflow volume is followed from an earlier "inflow time" shown in Fig. 5 corresponding to the start of the MetUM forecasts.
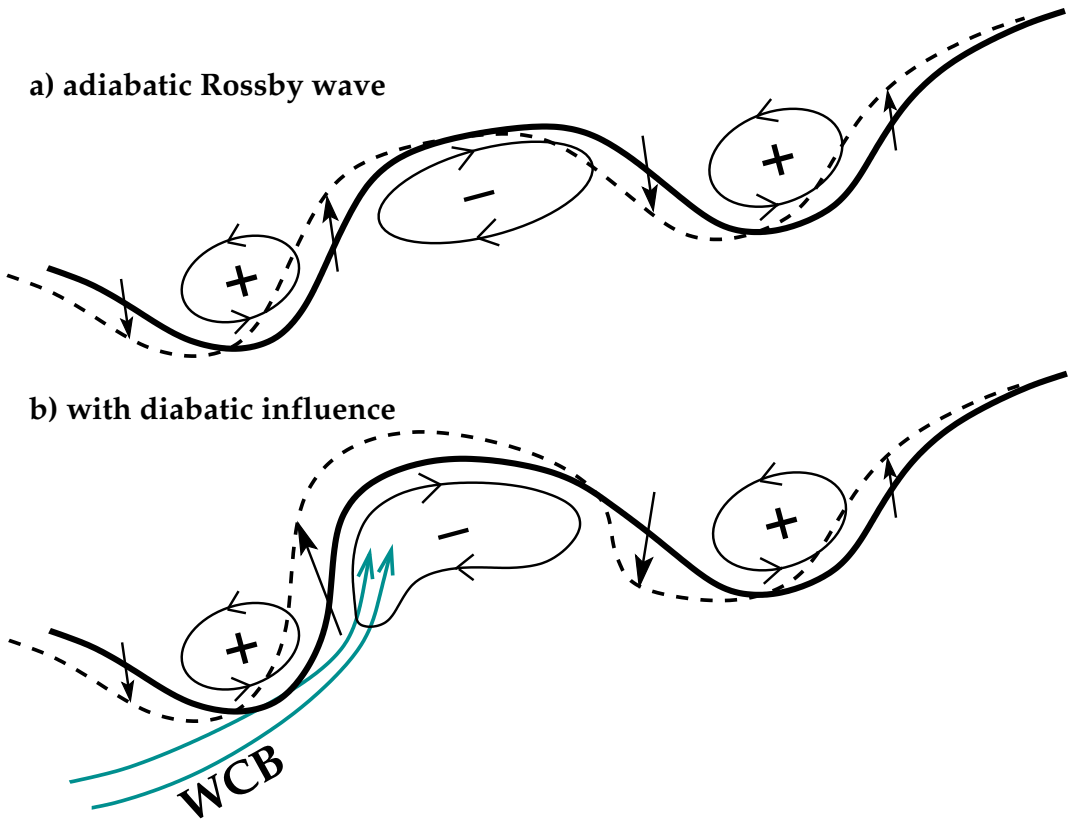
FIGURE 9 A schematic showing the impact of diabatic effects in a WCB on a Rossby wave. a) Circulations self-induced by the PV anomalies of an adiabatic Rossby wave and consequent westward propagation of the pattern. b) Distortion of the wave shape arising from diabatic mass transport in the WCB: nonlinear advection of the tropopause by divergent outflow on the western flank of the ridge and the effect additional anticyclonic vorticity on its eastern flank.

4.6 | Role of WCB outflow in Rossby wave evolution

How do the changes in the WCB outflow volume then go on to influence the Rossby wave evolution? Figure 9 illustrates the typical influences of diabatic processes on the structure of a Rossby wave at tropopause level. Panel (a) presents the canonical situation of an adiabatic Rossby wave (Hoskins et al., 1985). The bold contour represents an isoline of PV situated within the strong PV gradient zone associated with the jet stream. Where air has been displaced northwards (up the page) it has lower PV values compared with its surroundings because PV is materially conserved and has a positive meridional gradient. Through inversion, the negative PV anomaly is associated with anticyclonic relative vorticity as well as lower static stability. Where air has been displaced southwards it has a positive PV anomaly which is associated with cyclonic relative vorticity through PV inversion. The meridional (cross-jet) motion induced by the chain of vorticity anomalies results in displacement of the PV contours through advection to give rise to the dashed contour a short time later. The net result of the induced motion is to propagate the PV wave pattern towards the west; the Rossby wave propagation mechanism. At the same time the strong westerly flow associated with the jet stream (and the existence of the PV gradient) advects the whole pattern eastwards. For wavelengths characteristic of synoptic scale waves, zonal

advection by the basic flow is stronger than propagation and so the pattern translates eastwards, but at a slower speed than the jet stream flow.

There are several key points about the adiabatic situation shown. The flow self-induced by the PV anomalies is directly in the cross-jet direction at the nodes between the vorticity anomalies. If the PV-wave were sinusoidal, then the self-induced meridional wind pattern would also be sinusoidal but shifted 90 degrees in phase to the east. Therefore, the linear response to the wave pattern in isolation would be for it to propagate without changing shape. In the schematic the positive anomalies are shown deliberately narrower than the negative anomalies. This behaviour is predicted by semi-geostrophic theory (e.g. Hoskins and James (2014)) where the advection of dynamic variables by the ageostrophic wind is included (in contrast to quasi-geostrophic theory where there is symmetry between the cyclonic and anticyclonic anomalies). The disturbance is typically part of a baroclinic wave, representing the upper counter-propagating Rossby wave (CRW) with PV anomalies focused at tropopause-level (Heifetz et al., 2004). The meridional wind induced by a lower CRW, existing on the low level meridional temperature gradient, can result in growth, decay or change in the propagation rate of the upper CRW. However, while central to growth, the winds induced by the lower CRW at tropopause-level are much weaker that the winds self-induced by the upper CRW and so are not explicitly represented in this schematic.

Panel (b) illustrates how the symmetry is disturbed and the wave structure changed through diabatic influence. The WCB air stream ascends to the level of the upper Rossby wave and transports mass diabatically into the outflow volume which is already characterised by lower PV than average (due to the meridional displacement of air). The increase in outflow mass results in even lower static stability, but also in divergent horizontal outflow. The additional divergent flow typically results in a greater component of velocity oriented across the PV gradient from troposphere towards stratosphere on the western flank of the ridge (Grams and Archambault, 2016; Sánchez et al., 2020). Additionally, the enhanced anticyclonic vorticity associated with the outflow area increase (item 1 above) turns the downstream wind vectors anticyclonically. In our case studies, we found that the changes in vorticity are typically much larger than the changes in static stability and the contribution to this from area expansion is comparable to the change due to meridional displacement (Table 2). The net result of nonlinear advection is to produce the dashed curve where the ridge is typically distorted so that its northwest flank expands while its eastern flank wraps anti-cyclonically.

This schematic matches closely the structure of Rossby wave composites obtained for forecast bust flow situations by Grams et al. (2018). The forecast busts are associated with a tendency to under-predict the onset of dipole blocking on the downstream side of a ridge. Sánchez et al. (2020) have shown that predictability barriers, characterized by the faster growth of ensemble mean error than ensemble spread, are associated strongly with enhanced diabatic influence on tropopause advection. The sense of the error in the cases shown there is that the ridge expansion and anticyclonic turning downstream are both under-predicted, and at the same time diabatic influence is too weak in the forecasts for lead times greater than two days such that forecasts at longer lead times look more like panel (a).

5 | CONCLUSIONS

The purpose of this work was to examine the ways in which latent heating and diabatic mass transport within the warm conveyor belt (WCB) of cyclones can alter the evolution of Rossby waves on the jet stream at tropopause level. WCBs typically transport air polewards and their outflow enters the upper troposphere on the western and northern flank of ridges in Rossby waves. The WCB outflow has anomalously low PV compared with air elsewhere at the same latitude and isentropic surface. However, the PV impermeability theorem of Haynes and McIntyre (1987, 1990) shows exactly that there can be no flux of PV across isentropic surfaces at any point (see Eq. 5). This raises a conundrum: how
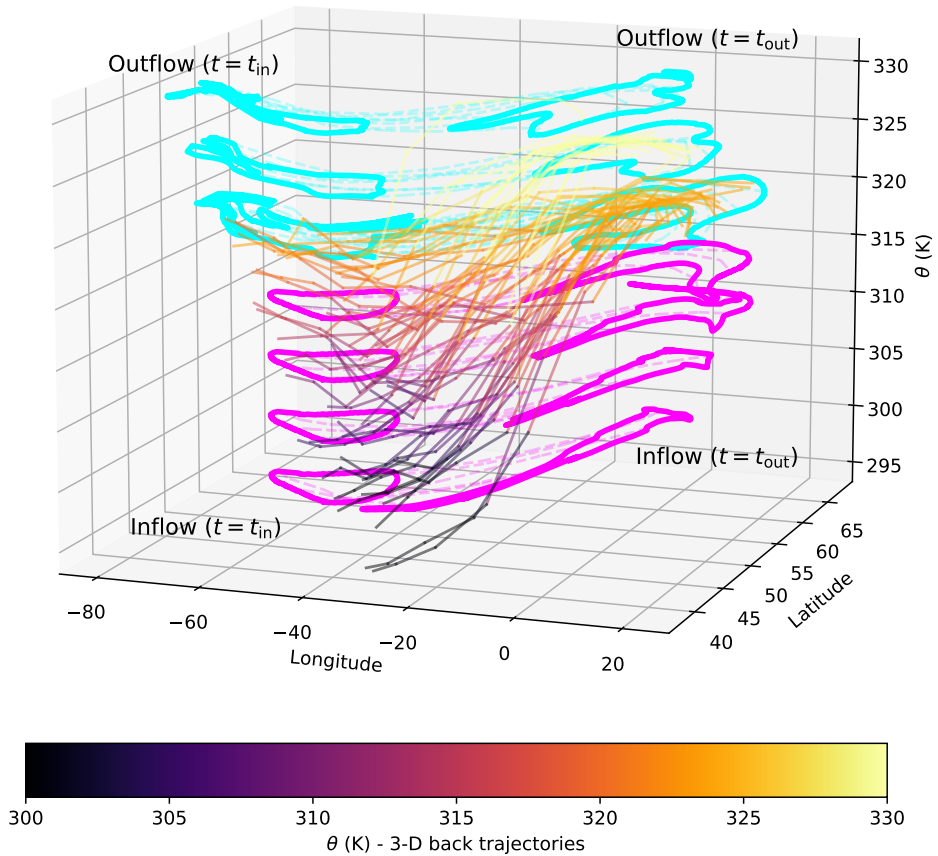
FIGURE 10 A realisation of the schematic in Fig. 1 from Methven (2015) using data from IOP3. The cyan contours show the outflow volume (on isentropic surfaces 325K ±5 K). The dashed cyan lines show the isentropic back trajectories (every 50th) tracing the boundary of the outflow volume at the outflow time, t_{out}, back to the inflow time, t_{in}. The coloured lines show the 3-D back trajectories (every 250th) from gridpoints within the outflow volume at the outflow time, t_{out}, that trace back to below 320K at the inflow time, t_{in} and are considered WCB trajectories. The magenta contours show the inflow volume (on isentropic surfaces 300-315 K) determined as the area enclosing the horizontal projection of the majority of the WCB trajectories at the inflow time, t_{in}. The dashed magenta lines show the isentropic forward trajectories (every 50th) tracing the boundary of the inflow volume at the inflow time, t_{in}, forward to the outflow time, t_{out}.

can diabatic mass transport influence Rossby wave patterns and their evolution if there can be no flux of PV across isentropic surfaces?

The problem is examined by identifying the WCB outflow at "outflow time", t_{out}, as bounding air in an upper tropospheric ridge that has experienced net heating over the last few days. Back trajectories were calculated from this WCB outflow using two approaches. Isentropic back trajectories from the lateral boundary of the outflow were used to trace an "outflow volume" backwards in time, this control volume being constrained to remain within the isentropic layer. Back trajectories using the full 3-D winds resolved by the MetUM were calculated from all grid-points within the outflow volume to trace the WCB air mass backwards in time. Then the integral properties of the outflow volume are calculated including circulation, average potential vorticity (PV), isentropic density, areal extent and average relative vorticity. The calculations are framed in terms of the conceptual model of WCBs proposed by Methven (2015) (see Fig. 1) and one aim is to investigate the extent to which the conceptual model, and the implications that stem from it, are applicable to diverse WCB cases. Figure 10 is a realisation of the schematic using model data from the NAWDEX IOP3 case study illustrating that it is possible to identify WCB outflow and inflow volumes and test the predictions of the theory.

Five specific questions were posed following the development of the theory in Section 2 and conclusions will now be drawn on each question in turn:

1. **What fraction of mass in the WCB outflow volume (at the outflow time) arrived by diabatic mass transport?**
   Outflow volumes were defined using a θ-tracer running online within the MetUM to identify coherent regions that have experienced net diabatic heating during the forecast. The smoothed boundary of such regions defined the lateral boundary of the outflow and the "outflow time" (t_{out}) was associated with a marked decline in heating active within the WCB, but before another WCB affected the same synoptic scale ridge. The proportion of outflow air experiencing diabatic mass transport varies greatly between cases. During NAWDEX, which was an active season characterised by Rossby wave breaking events with low predictability (Schäfler et al., 2018; Sánchez et al., 2020), the events with greatest diabatic mass transport were the Vladiana Cyclone (IOP3) and the rapidly deepening Stalactite Cyclone (IOP6). In these cases the mass of the isentropic "outflow volume" increased by 40-60% (relative to inflow time) by diabatic mass transport into the volume from below in the WCB. Across the cases examined, and depending on the isentropic layers considered, the diabatic mass transport fraction varied between 10% and 80%.

2. **How well is the outflow volume circulation conserved?**
   In the cases examined, the fractional change in circulation, between the inflow and outflow time, varied by less than 15%. The size of variation is no larger than inconsistency between numerical estimates from the circuit integral of velocity around the outflow volume, or an area integral of vorticity on isentropic surfaces within the volume. Circulation was less well conserved in the top isentropic layer of the identified "outflow volumes" and this was attributed to small-scale noise in the model PV field associated with partially resolved gravity wave activity.

3. **What is the geometry of the inflow volume (at inflow time) enclosing air that subsequently ascends in the WCB?**
   An "inflow time" was identified with the beginning of substantial diabatic heating within the WCB. The WCB was identified with the trajectory subset that originated from below the isentropic layer of the outflow, at inflow time. The lateral boundary of the "inflow volume" was defined as an envelope surrounding the horizontal locations of the WCB trajectory ensemble at inflow time. A surprising finding was that, at the inflow time, the lateral boundaries of the outflow and inflow volumes are similar to the extent that the areas associated with the horizontal projections of both volumes are largely over-lapping. This was true in all the cases examined. However, in contrast to the conceptual model, the origin of WCB trajectories was spread over a large vertical extent rather than being confined to a shallow isentropic layer at low levels.

4. **Under what circumstances does the average PV of the outflow approximately equal the PV of the inflow?**

   The core of the explanation relates to two properties of the circulation integrals. Firstly, at the inflow time the circulation integrals around the inflow and outflow lateral boundaries are approximately equal, deduced from the fact that the horizontal projections of the two volumes are similar and follow each other for a few hours after inflow time. However, this is not a rigorous argument and the relationship is only approximate. Secondly, the circulation of the outflow volume is conserved as a consequence of the PV impermeability theorem (or Kelvin's circulation theorem generalised to include diabatic and frictional processes). Therefore, the circulation of the outflow approximately equals the circulation of the inflow (at inflow time). In some cases, there is some freedom to vary the inflow volume boundaries such that the mass of the inflow (at initial time) equals the mass of the outflow (at final time) and also the isentropic layer thickness of the two volumes is the same ($\Delta\theta_1 = \Delta\theta_2$) while still meeting the constraint that the inflow encompasses most of the CET that will end up in the outflow. Bringing all these points together, a consequence is that (15) can be approximately satisfied and the average PV of the outflow approximately equals the PV of the inflow in IOP5 and IOP7. In IOP3 and IOP6, the average PV of the outflow (at outflow time) is lower than the PV of the inflow (at inflow time). This is because the 3-D WCB trajectories span a deeper isentropic layer at "inflow time" ($\Delta\theta_1$) than the outflow layer depth ($\Delta\theta_2$) so that even though the circulation of the upper isentropic volume is conserved and it is approximately possible to identify an inflow volume satisfying $M_1(t_{\text{in}}) \approx M_2(t_{\text{out}})$, Eqn. (15) indicates that the average PV of the upper volume is smaller.

5. **If the outflow circulation integral is unchanged by diabatic processes, in what ways can heating in a WCB influence Rossby waves?**

   Although the circulation integral of the outflow volume is approximately invariant, the diabatic mass transport into the volume has several major effects:

   a. The influx of mass into the notional outflow volume from below is partitioned between an increase in density in isentropic coordinates (a decrease in static stability) and an increase in outflow area (due to additional divergence in the horizontal flow). Due to conservation of circulation, the increase in area must be associated with a decrease in average absolute vorticity and therefore increasingly anticyclonic relative vorticity in the outflow. It is this relative vorticity change that affects large-scale Rossby wave evolution near tropopause level.

   b. The mass influx also dilutes PV substance in the volume resulting in a decrease in average PV. PV inversion associated with balanced dynamics dictates that the partition between vorticity and stratification anomalies is approximately even if the PV anomaly of outflow volume has an aspect ratio such that $NH/(fL) \approx 1$. Since the fractional area change is equal and opposite to the fractional vorticity change, balance predicts that the area increase of the outflow must be less than the mass increase.

   c. Diabatic mass transport deposits the WCB outflow on higher isentropic surfaces than would be accessed in an adiabatic situation. Therefore the low PV characterising the outflow is more anomalously negative compared with its surroundings at the same latitude and altitude and for this reason might be expected to have greater influence on the flow.

   d. The structure of baroclinic waves is such that the anticyclonic branch of the WCB is more dominant than the cyclonic branch on higher isentropic surfaces (as suggested by Thorncroft et al. (1993)). Martínez-Alvarado et al. (2014) has shown by comparing different models and convection schemes that simulations with greater net heating do indeed exhibit a greater proportion of mass in the anticyclonic WCB branch. Therefore, latent heating within WCBs has a fundamental influence on the nonlinear wave breaking behaviour of the baroclinic waves in which they are embedded.

   e. Although heating within the outflow volume, or diabatic mass transport from below, cannot affect the circulation integral, it can change the distribution of PV and local flow anomalies that can distort the shape of the outflow

volume with ramifications for perturbations to the tropopause position and downstream propagation of wave activity. For example, Oertel et al. (2020) show, in convection-permitting simulations of NAWDEX IOP3, that horizontal PV dipoles produced by convective heating in large-scale vertical wind shear tend to aggregate into long PV dipole strips within the WCB outflow. Since the negative pole must always be nearer the jetstream core (as shown by Harvey et al. (2020)) it is advected faster and as the negative and postive strips separate vortex roll-up at the ends of the strips can distort the tropopause shape, tending to create a local jet streak and tropopause-level perturbation.

Note that the identification of the WCB outflow in this study differed from the typical identification of WCBs using trajectories (Wernli and Davies, 1997; Madonna et al., 2014). This is because the aim here was to consider the entire air mass in the outflow, not only air parcels experiencing deep ascent. In our cases we found many air parcels that ascended into the outflow but did not originate in the atmospheric boundary layer and therefore had weaker ascent than the threshold typically used for identification of WCBs. However, our definition of inflow, ascent, and outflow times are fixed times for each WCB case, whereas, when identifying WCBs from trajectories, these times would be defined for each individual trajectory such that inflow, ascent, and outflow can occur at the same time for different trajectories within a single WCB. Nevertheless, the origin of mass diabatically ascending into the outflow layer was spread over a large depth of the lower troposphere. We attempted to use cluster analysis, following Hart et al. (2015), to objectively identify the WCB trajectories but did not convincingly distinguish a separate cluster of trajectories with stronger ascent. However, a better choice of metric and reference frame may improve this clustering (e.g. Kremer et al. (2020)).

The definition of inflow, ascent and outflow times were also constrained by how far back we could track the outflow volume. Although, by definition, trajectories on constrained to isentropic surfaces should not cross, numerical issues led to convoluted contours that gave inconsistent estimates for the circulation. Increasing the temporal resolution of the winds used for the trajectory calculations should improve this issue. A more complicated, but perhaps more useful, method in the future could also be to use a contour advection method that adjust the nodes around the contour to keep a consistent resolution (Waugh and Plumb, 1994).

Figure 9 presents a schematic summary of the influence of diabatic mass transport in WCBs on the structure of upper-level Rossby waves and the associated meanders of the jet stream, compared with a notional adiabatic flow situation. In brief, diabatic mass transport into the outflow isentropic layer results in a stronger negative PV anomaly, expansion in outflow area, especially on the western flank of ridges, stronger anticyclonic relative motion and a greater propensity for anti-cyclonic turning of PV contours downstream of the ridge.

It is remarkable that in these WCBs cases, with diverse structure and heating intensity, at the inflow time the horizontal projection of the isentropic outflow volume largely overlaps the inflow volume. The implication is that the coherent ensemble of 3-D trajectories defining the WCB mass transport follow more or less beneath the "shadow" of the outflow volume traced backwards within the isentropic layer of the outflow (Fig. 10). There is large vertical and horizontal wind shear beneath the jet stream and also across the cold front that neighbours the WCB air stream. Typically, WCB trajectories slide slantwise up the sloping frontal surface as they experience latent heating. It must be the case that the wind shear evaluated along the frontal surface between the isentropic outflow layer and the level of trajectories within the WCB is not too great, otherwise the difference in horizontal tracks would not be such a small fraction of the total distance travelled by the trajectories (Fig. 4). This can be explained partly because the WCB trajectories remain on the warm side of the main shear of the cold frontal interface at all times.

The conclusions regarding the influence of WCBs on the large-scale flow and Rossby wave development are insensitive to the finescale details of vertical motion within the WCB, including embedded convection. While a trace constituent, with mixing ratio q, would in general experience a diabatic flux across isentropic surfaces, $\rho q \mathbf{u}_D$, the PV

impermeability theorem shows that PV behaves in a fundamentally different way and has precisely zero flux normal to isentropic surfaces (Eq. 5). Convection or other motions, where heating occurs in updrafts, would be expected to result in a diabatic tracer flux $\overline{\rho q' \mathbf{u}_D'}$ where the overbar denotes an area average on an isentropic surface. If there is a bulk gradient in tracer concentration with respect to potential temperature, and the correlation length (in terms of θ) of the turbulent motions is relatively short, then a down-gradient cross-isentropic turbulent flux is expected (Sparling et al., 1997). For example, Purvis et al. (2003) have shown observational evidence for the rapid uplift of short-lived hydrocarbon pollution (decay timescales of hours to days) in a WCB crossing western Europe. The concentration of these compounds above the boundary layer is strongly dependent on embedded convective updrafts within the WCB because transport is much faster within the updrafts. In contrast, there must be precisely zero cross-isentropic PV flux at any location. This is important because the occurrence of embedded mid-level convection is common but highly variable between cases. For example, Oertel et al. (2020) found that 77% of WCB trajectories in their convection-permitting simulation of IOP3 passed through convective cloud at some point. Blanchard et al. (2020) showed how all observed convection with updrafts reaching WCB outflow level in IOP6 initiated at mid-levels within the WCB. While this mid-level convection can create large amplitude PV dipoles and associated flow anomalies (Oertel and Schemm, 2021), the key here is to be able to define an outflow boundary lying outside the heating on most of the circuit such that the effect of these PV dipoles on circulation integrates to zero.

Note that no approximations to the fluid dynamical equations are used to arrive at the PV impermeability theorem (5) and its integral form (9). Therefore, all that matters to the large-scale dynamics of the WCB problem is the net latent heating that enables bulk diabatic transport of mass into the outflow isentropic layer. As long the inflow volume can be defined that contains all the mass at the inflow time that subsequently ends up in the outflow volume through the diabatic pathway, the arguments related to invariance of outflow circulation and consequences for Rossby wave vorticity anomalies hold. By defining inflow air to originate from any isentropic surfaces beneath the outflow layer, combined with the observation from the NAWDEX simulations that the outflow volume (traced back in time but constrained to an isentropic layer) largely overshadows the horizontal projection of the 3-D WCB back trajectories, it is clear that any air that experiences sufficient heating, whether it be through large-scale ascent and condensation or in a convective updraft, will transport mass from the inflow to the outflow volume. Therefore, it is expected that the representation of diabatic influence on circulation and Rossby wave dynamics is relatively insensitive to the partition between resolved and sub-grid velocity in models and their variation with model resolution, compared with the dependence of passive tracer transport. However, the diabatic influence on dynamics will depend on the representation of net heating which can differ greatly between models with parametrized or explicitly simulated convection, as indicated by the differences in precipitation rates and accumulations in many flow regimes.

ACKNOWLEDGEMENTS

ENDNOTES

REFERENCES

Ahmadi-Givi, F., Craig, G. C. and Plant, R. S. (2004) The dynamics of a midlatitude cyclone with very strong latent-heat release. *Q. J. R. Meteorol. Soc.*, **130**, 295–323.

Blanchard, N., Pantillon, F., Chaboureau, J.-P. and Delanoë, J. (2020) Organization of convective ascents in a warm conveyor belt. *Weather Clim. Dynam.*, **1**, 617–634.

— (2021) Mid-level convection in a warm conveyor belt accelerates the jet stream. *Weather Clim. Dynam.*, **2**, 37–53.

Bland, J. (2018) *Circulation in the Outflow of Warm Conveyor Belts.* Master's thesis, Dept. of Meteorology, University of Reading.

Bretherton, F. P. (1966) Baroclinic instability and the short wavelength cut-off in terms of potential vorticity. *Q. J. R. Meteorol. Soc.*, **92**, 335–345.

Chagnon, J. M., Gray, S. L. and Methven, J. (2013) Diabatic processes modifying potential vorticity in a North Atlantic cyclone. *Q. J. R. Meteorol. Soc.*, **139**, 1270–1282.

De Vries, H., Methven, J., Frame, T. H. A. and Hoskins, B. J. (2010) Baroclinic Waves with Parameterized Effects of Moisture Interpreted Using Rossby Wave Components. *J. Atmos. Sci.*, **67**, 2766–2784.

Emanuel, K. A., Fantini, M. and Thorpe, A. J. (1987) Baroclinic Instability in an Environment of Small Stability to Slantwise Moist Convection. Part I: Two-Dimensional Models. *J. Atmos. Sci.*, **44**, 1559–1573.

Grams, C. M. and Archambault, H. M. (2016) The key role of diabatic outflow in amplifying the midlatitude flow: a representative case study of weather systems surrounding western North Pacific extratropical transition. *Mon. Weather Rev.*, **144**, 3847–3869.

Grams, C. M., Magnusson, L. and Madonna, E. (2018) An atmospheric dynamics perspective on the amplification and propagation of forecast error in numerical weather prediction models: A case study. *Q. J. R. Meteorol. Soc.*, **144**, 2577–2591.

Grams, C. M., Wernli, H., Böttcher, M., Čampa, J., Corsmeier, U., Jones, S. C., Keller, J. H., Lenz, C. J. and Wiegand, L. (2011) The key role of diabatic processes in modifying the upper-tropospheric wave guide: A North Atlantic case-study. *Q. J. R. Meteorol. Soc.*, **137**, 2174–2193.

Harrold, T. W. (1973) Mechanisms influencing the distribution of precipitation within baroclinic disturbances. *Q. J. R. Meteorol. Soc.*, **99**, 232–251.

Hart, N. C. G., Gray, S. L. and Clark, P. A. (2015) Detection of coherent airstreams using cluster analysis: Application to an extratropical cyclone. *Mon. Weather Rev.*, **143**, 3518–3531.

Harvey, B., Methven, J., Sanchez, C. and Schäfler, A. (2020) Diabatic generation of negative potential vorticity and its impact on the North Atlantic jet stream. *Q. J. R. Meteorol. Soc.*, **146**, 1477–1497.

Haynes, P. H. and McIntyre, M. E. (1987) On the Evolution of Vorticity and Potential Vorticity in the Presence of Diabatic Heating and Frictional or Other Forces. *J. Atmos. Sci.*, **44**, 828–841.

— (1990) On the Conservation and Impermeability Theorems for Potential Vorticity. *J. Atmos. Sci.*, **47**, 2021–2031.

Heifetz, E., Methven, J., Hoskins, B. J. and Bishop, C. H. (2004) The counter-propagating Rossby-wave perspective on baroclinic instability. I: Mathematical Basis. *Q. J. R. Meteorol. Soc.*, **130**, 211–231.

Hoskins, B. and James, I. N. (2014) *Fluid dynamics of the midlatitude atmosphere.* Wiley Blackwell.

Hoskins, B. J., McIntyre, M. E. and Robertson, A. W. (1985) On the use and significance of isentropic potential vorticity maps. *Q. J. R. Meteorol. Soc.*, **111**, 877–946.

Kremer, T., Schömer, E., Euler, C. and Riemer, M. (2020) Cluster Analysis Tailored to Structure Change of Tropical Cyclones Using a Very Large Number of Trajectories. *Mon. Weather Rev.*, **148**, 4209–4229.

Maddison, J. W., Gray, S. L., Martínez-Alvarado, O. and Williams, K. D. (2019) Upstream Cyclone Influence on the Predictability of Block Onsets over the Euro-Atlantic Region. *Mon. Weather Rev.*, **147**, 1277–1296.

Madonna, E., Wernli, H., Joos, H. and Martius, O. (2014) Warm conveyor belts in the ERA-Interim Dataset (1979-2010). Part I: Climatology and potential vorticity evolution. *J. Clim.*, **27**, 3–26.

Martínez-Alvarado, O., Baker, L. H., Gray, S. L., Methven, J. and Plant, R. S. (2014) Distinguishing the Cold Conveyor Belt and Sting Jet Airstreams in an Intense Extratropical Cyclone. *Mon. Weather Rev.*, **142**, 2571–2595.

Martínez-Alvarado, O., Madonna, E., Gray, S. L. and Joos, H. (2016) A route to systematic error in forecasts of Rossby waves. *Q. J. R. Meteorol. Soc.*, **142**, 196–210.

Methven, J. (2015) Potential vorticity in warm conveyor belt outflow. *Q. J. R. Meteorol. Soc.*, **141**, 1065–1071.

Methven, J., Heifetz, E., Hoskins, B. J. and Bishop, C. H. (2005) The counter-propagating Rossby-wave perspective on baroclinic instability. Part III: Primitive equations on the sphere. *Q. J. R. Meteorol. Soc.*, **131**, 1393–1424.

Oertel, A., Boettcher, M., Joos, H., Sprenger, M., Konow, H., Hagen, M. and Wernli, H. (2019) Convective activity in an extra-tropical cyclone and its warm conveyor belt – a case-study combining observations and a convection-permitting model simulation. *Q. J. R. Meteorol. Soc.*, **145**, 1406–1426.

Oertel, A., Boettcher, M., Joos, H., Sprenger, M. and Wernli, H. (2020) Potential vorticity structure of embedded convection in a warm conveyor belt and its relevance for large-scale dynamics. *Weather Clim. Dynam.*, **1**, 127–153.

Oertel, A. and Schemm, S. (2021) Quantifying the circulation induced by convective clouds in kilometer-scale simulations. *Q. J. R. Meteorol. Soc.*, **147**, 1752–1766.

Pfahl, S., Schwierz, C., Croci-Maspoli, M., Grams, C. M. and Wernli, H. (2015) Importance of latent heat release in ascending air streams for atmospheric blocking. *Nat. Geosci.*, **8**, 610–614.

Purvis, R. M., Lewis, A. C., Carney, R. A., McQuaid, J. B., Arnold, S. R., Methven, J., Barjat, H., Dewey, K., Kent, J., Monks, P. S., Carpenter, L. J., Brough, N., Penkett, S. A. and Reeves, C. E. (2003) Rapid uplift of nonmethane hydrocarbons in a cold front over central Europe. *J. Geophys. Res. Atmos.*, **108**.

Sánchez, C., Methven, J., Gray, S. and Cullen, M. (2020) Linking rapid forecast error growth to diabatic processes. *Q. J. R. Meteorol. Soc.*, **146**, 3548–3569.

Schäfler, A., Craig, G., Wernli, H., Arbogast, P., Doyle, J. D., McTaggart-Cowan, R., Methven, J., Rivière, G., Ament, F., Boettcher, M., Bramberger, M., Cazenave, Q., Cotton, R., Crewell, S., Delanoë, J., Dörnbrack, A., Ehrlich, A., Ewald, F., Fix, A., Grams, C. M., Gray, S. L., Grob, H., Groß, S., Hagen, M., Harvey, B., Hirsch, L., Jacob, M., Kölling, T., Konow, H., Lemmerz, C., Lux, O., Magnusson, L., Mayer, B., Mech, M., Moore, R., Pelon, J., Quinting, J., Rahm, S., Rapp, M., Rautenhaus, M., Reitebuch, O., Reynolds, C. A., Sodemann, H., Spengler, T., Vaughan, G., Wendisch, M., Wirth, M., Witschas, B., Wolf, K. and Zinner, T. (2018) The North Atlantic Waveguide and Downstream Impact Experiment. *Bull. Am. Meteorol. Soc.*, **99**, 1607–1637.

Schemm, S., Wernli, H. and Papritz, L. (2013) Warm Conveyor Belts in Idealized Moist Baroclinic Wave Simulations. *J. Atmos. Sci.*, **70**, 627–652.

Sparling, L. C., Kettleborough, J. A., Haynes, P. H., McIntyre, M. E., Rosenfield, J. E., Schoeberl, M. R. and Newman, P. A. (1997) Diabatic cross-isentropic dispersion in the lower stratosphere. *J. Geophys. Res. Atmos.*, **102**, 25817–25829.

Sprenger, M. and Wernli, H. (2015) The LAGRANTO Lagrangian analysis tool – version 2.0. *Geosci. Model Dev.*, **8**, 2569–2586.

Thorncroft, C. D., Hoskins, B. J. and McIntyre, M. E. (1993) Two paradigms of baroclinic-wave life-cycle behaviour. *Q. J. R. Meteorol. Soc.*, **119**, 17–55.

Walters, D., Boutle, I., Brooks, M., Melvin, T., Stratton, R., Vosper, S., Wells, H., Williams, K., Wood, N., Allen, T., Bushell, A., Copsey, D., Earnshaw, P., Edwards, J., Gross, M., Hardiman, S., Harris, C., Heming, J., Klingaman, N., Levine, R., Manners, J., Martin, G., Milton, S., Mittermaier, M., Morcrette, C., Riddick, T., Roberts, M., Sanchez, C., Selwood, P., Stirling, A., Smith, C., Suri, D., Tennant, W., Vidale, P. L., Wilkinson, J., Willett, M., Woolnough, S. and Xavier, P. (2017) The Met Office Unified Model Global Atmosphere 6.0/6.1 and JULES Global Land 6.0/6.1 configurations. *Geosci. Model Dev.*, **10**, 1487–1520.

Waugh, D. W. and Plumb, R. A. (1994) Contour advection with surgery: A technique for investigating finescale structure in tracer transport. *J. Atmos. Sci.*, **51**, 530–540.

Wernli, H. and Davies, H. C. (1997) A lagrangian-based analysis of extratropical cyclones. I: The method and some applications. *Q. J. R. Meteorol. Soc.*, **123**, 467–489.

Wood, N., Staniforth, A., White, A., Allen, T., Diamantakis, M., Gross, M., Melvin, T., Smith, C., Vosper, S., Zerroukat, M. and Thuburn, J. (2014) An inherently mass-conserving semi-implicit semi-Lagrangian discretization of the deep-atmosphere global non-hydrostatic equations. *Q. J. R. Meteorol. Soc.*, **140**, 1505–1520.